Radar observations and a physical model of binary near-Earth asteroid 65803 Didymos, target of the DART mission

S.P. Naidu [a,*], L.A.M. Benner [a], M. Brozovic [a], M.C. Nolan [b], S.J. Ostro [a,1], J.L. Margot [c], J. D. Giorgini [a], T. Hirabayashi [d], D.J. Scheeres [e], P. Pravec [f], P. Scheirich [f], C. Magri [g], J.S. Jao [a]

[a] Jet Propulsion Laboratory, California Institute of Technology, Pasadena, CA, United States of America
[b] Lunar and Planetary Laboratory, University of Arizona, Tucson, AZ, United States of America
[c] Department of Earth, Planetary, and Space Sciences, University of California, Los Angeles, CA, United States of America
[d] Department of Aerospace Engineering, Auburn University, Auburn, AL, United States of America
[e] Department of Aerospace Engineering, University of Colorado, Boulder, CO, United States of America
[f] Astronomical Institute, Academy of Sciences of the Czech Republic, Ondrejov, Czech Republic
[g] University of Maine, Farmington, ME, United States of America

ARTICLE INFO

ABSTRACT

Near-Earth asteroid Didymos is a binary system and the target of the proposed Double Asteroid Redirection Test (DART) mission (Cheng et al., 2016), which is a planetary defense experiment. The DART spacecraft will impact the satellite, causing changes in the binary orbit that will be measured by Earth-based observers. We observed Didymos using the planetary radars at Arecibo (2380 MHz, 12.6 cm) and Goldstone (8560 MHz, 3.5 cm) in November 2003. Delay-Doppler radar imaging of the binary system provided range resolutions of up to 15 m/ pixel that placed hundreds of pixels on the primary. We used the radar data to estimate a 3D shape model and spin state for the primary, the secondary size and spin, the mutual orbit parameters, and the radar scattering properties of the binary system. We included lightcurves obtained by Pravec et al. (2006) in the shape model estimation. The primary is top-shaped with an equatorial bulge, a conspicuous facet along the equator, and a volume-equivalent diameter of 780 ± 30 m. The extents along the three principal axes are 832 m, 838 m, and 786 m, (uncertainties are 6% along the x and y axes, and 10% along the z axis). The radar data do not provide complete rotational coverage of the secondary but show visible extents of about 75 m, implying a diameter of 150 ± 30 m. The bandwidth of the secondary in the images suggests a spin period of 12.4 ± 3.0 h that is consistent with rotation that is synchronized with the mutual orbit period of 11.9 h. We fit a mutual orbit to the system using the delay and Doppler separations between the binary components and obtain a semimajor axis of 1190 ± 30 m, an eccentricity of <0.05, and an orbital period of 11.93 ± 0.01 h that are consistent with those obtained by Scheirich and Pravec (2009) and Fang and Margot (2012). The mutual orbit implies a system mass of $(5.4 \pm 0.4) \times 10^{11}$ kg and a system bulk density of 2170 ± 350 kg m^{-3}. The system has S- and X-band radar albedos of 0.20 ± 0.05 and 0.30 ± 0.08 respectively, and an optical albedo of 0.15 ± 0.04.

1. Introduction

Binary near-Earth asteroid (NEA) 65803 Didymos (1996 GT) was discovered on April 11, 1996 by the Spacewatch telescope at Kitt Peak. The binary system has a mean absolute magnitude (when not undergoing mutual events) of 18.16 ± 0.04 (Pravec et al., 2012) and was the subject of numerous optical observing campaigns during an approach within 0.048 au in November 2003. We observed Didymos using the Goldstone Solar System Radar (GSSR) on November 14 and 15 but did not detect the satellite, which was discovered later through mutual events seen in photometric data obtained from 2003 November 20–24 by Pravec et al. (2003) and confirmed shortly afterwards in Arecibo delay-Doppler radar images obtained on 2003 November 23 and 24. Reprocessed Goldstone data at higher frequency resolutions later showed the satellite but at much weaker signal to noise ratios (SNRs) than in the Arecibo data.

Table 1
Radar observations of Didymos.

Obs.	UT date yyyy-mm-dd	Start-stop (hhmmss-hhmmss)	P_{tx} (kW)	RTT (s)	Runs	Mode	Code	δr (m)	δf (Hz)	Orb. Sol.
G	2003-11-14	051823–053355	450	48	10	C	None		0.5	s21
		055740–060458			5	I	127	1500	12.3	S21
		070530–071430			6	I	127	1650	11.2	S21
		075123–081009			12	I	127	150	4	S23
		083002–091148			26	I	127	75	0.5	s23
G	2003-11-15	044424–050015	450	49	10	C	None		0.5	s25
		053015–063803			41	I	127	75	0.5	s25
		072759–073849			7	I	127	75	0.5	s25
		091123–093035			12	I	127	75	0.5	s25
A	2003-11-23	030104–031009	450	61	5	C	None		0.2	s27
		032359–045825			47	I	65,535	15	0.3	s27
A	2003-11-24	025524–030447	400	63	5	C	None		0.2	s27
		031505–050841			54	I	65,535	15	0.3	s27
A	2003-11-26	025252–030309	400	68	5	C	None		0.2	s27
		030743–051951			58	I	65,535	15	0.3	s27

Note - First column indicates the observatory: A for Arecibo and G for the DSS-14 antenna at Goldstone; Start-stop indicates the UTC start and stop times of the received echoes; RTT is the round-trip light travel time to the target in seconds; runs is the number of transmit-receive cycles in each setup, Mode is either C for CW echo power spectra or I for Imaging; Code is the length of the transmitted binary code; δr and δf indicate the range and frequency resolutions of the delay-Doppler data; and the last column indicates the orbit solution number of the ephemeris used for taking the data. On 2003-11-14, the first 22 runs of the 75 m range resolution imaging had weak signal-to-noise ratios due to errors in telescope pointing and are not used in the shape modeling.

Pravec et al. (2006) used lightcurve observations to estimate a primary synodic rotation period of 2.2593 ± 0.0001 h and a sidereal period of 2.2600 h. They measured a lightcurve amplitude of 0.08 ± 0.01 magnitudes, which suggested that the primary shape has a low elongation. Pravec et al. (2006) and Scheirich and Pravec (2009) found two solutions for the mutual orbit with orbit poles in the northern and southern ecliptic hemispheres. Their estimated mutual orbits have periods of about 11.91 h, a semimajor axis of 2.9 times the mean primary equatorial radius, and eccentricities of <0.16 and 0.03 (3-sigma upper limits) for the prograde and retrograde orbital solutions, respectively. They estimated the ratio of mean effective diameters of the secondary to the primary at equator-on aspect to be about 0.21–0.22 with an uncertainty of 0.02.

Fang and Margot (2012) used delay and Doppler separations estimated visually from the 2003 radar images to fit a mutual orbit to the system. They estimated a semimajor axis of 1.18 (+0.04/−0.02) km, an eccentricity of 0.04 (+0.05/−0.04), and a system mass of 5.24×10^{11} kg (± ~10%). They do not report a mutual orbit pole. In the present paper we used a more rigorous method to estimate the delay and Doppler separations, which yielded a mutual orbit consistent with the results reported by Fang and Margot (2012) but with somewhat smaller uncertainties.

Didymos is classified as an S-type asteroid (Cheng et al., 2018) based on vis-IR spectra obtained by De Leon et al., 2010. Its optical albedo has not yet been reported. It has the lowest delta-V among known binary near-Earth asteroids (https://echo.jpl.nasa.gov/~lance/delta_v/delta_v.rendezvous.html) and is the target of the Double Asteroid Redirection Test (DART) mission (Cheng et al., 2016), which will impact the satellite between September 30 and October 2, 2022 when the asteroid will approach within 0.07 au of Earth. The primary goal of the mission is to demonstrate the kinetic impact technique for deflection of an asteroid and to estimate the momentum transfer efficiency (β) of the impact. These goals will be achieved by post-impact ground-based radar and photometric observations of Didymos and modeling. The Light Italian

Cubesat for Imaging of Asteroids (LICIA cube), built by the Italian Space Agency (ASI), will be carried with the DART spacecraft for in situ observations of the impact (Pirrotta et al., 2019; Tortora and Di Tana, 2019). Didymos is also the target of the European Space Agency's proposed Hera mission, which will rendezvous several years after DART for post-impact characterization of the target (Michel et al., 2018).

In this paper, we combine Arecibo and Goldstone radar observations with lightcurve data from Pravec et al. (2006) to characterize the Didymos binary system. We present a detailed shape model of the primary, estimate the size of the secondary, the spin states of both components, the parameters of the binary mutual orbit, and radar scattering properties. We place limits on any additional undetected satellites in the system, study the mechanical properties of the primary, and describe the observational circumstances during the next radar observation window in 2022.

2. Radar observations

We observed Didymos using the Goldstone X-band (3.5 cm, 8560 MHz) radar on November 14 and 15, 2003 and the Arecibo S-band (12.6 cm, 2380 MHz) radar on November 23, 24, and 26, 2003 (Table 1). On each day we obtained ten runs of echo power spectra at Goldstone followed by delay-Doppler images and at Arecibo we obtained five runs of echo power spectra followed by images. Radar observations were carried out according to the methods described in Magri et al. (2007). For obtaining echo power spectra, a monochromatic circularly polarized wave was transmitted for the round-trip light time (RTT) toward the asteroid. Echoes in the same sense (SC) and opposite sense (OC) circular polarizations were received, sampled, and recorded. A single such transmit-receive cycle is referred to as a *run*. A Fourier transform was applied to the samples to obtain the echo power spectra in both polarizations. The bandwidth of the received signal is determined by the physical properties of the target and the frequency of the transmitted wave. For a spherical target with diameter (D) and spin period (P), the

Table 2
Lightcurve observations from Pravec et al. (2006) used for modeling the primary shape.

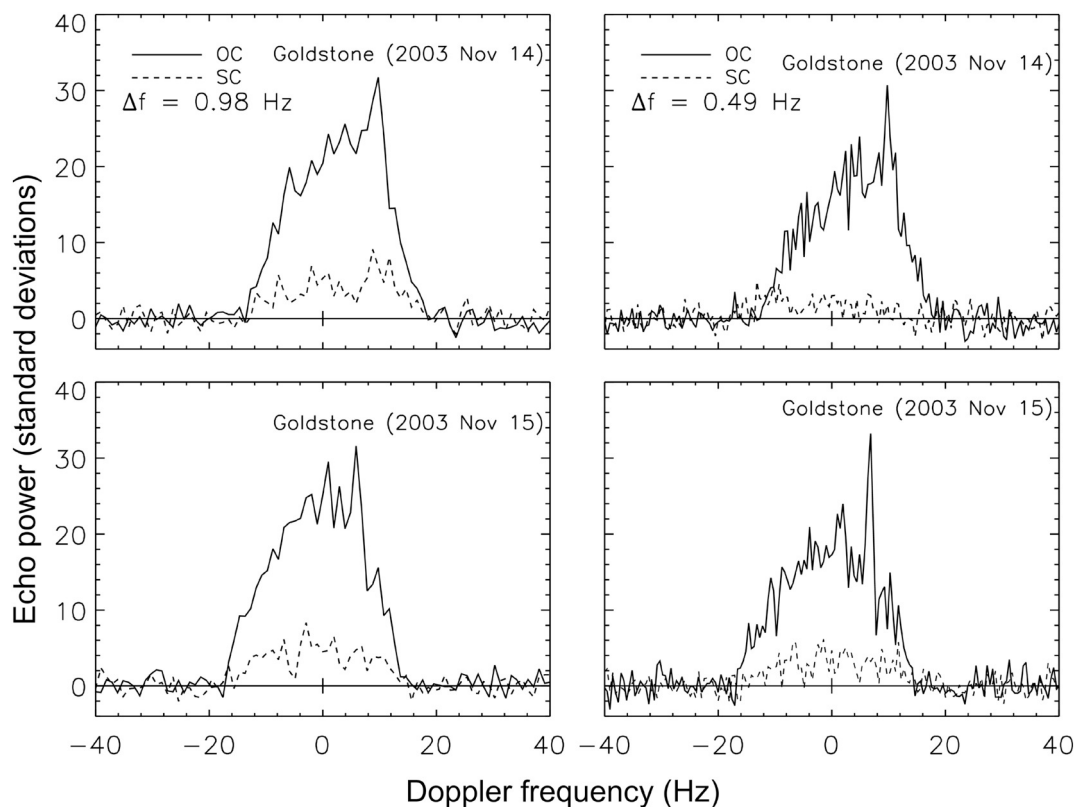| Pravec et al. (2006) Figure	Dates (UTC)	Dates (JD)	Apparent visual magnitude	Solar phase angles (degrees)	Number of data points
1	2003-11-20.89 to 11–24.37	2452964.39–2452967.87	12.9	19–12.6	771
2	2003-11-26.09 to 12–04.24	2452969.59–2452977.74	13.2	9.4–2.1	514
3	2003-12-16.83 to 12–20.46	2452990.33–2452993.96	14.9	7.4–9.2	374

Fig. 1. Single-day sums of echo power spectra obtained at Goldstone. The top and bottom panels show spectra obtained on Nov 14 and 15 respectively. The panels on the left and right have Doppler frequency resolutions of 0.98 Hz and 0.49 Hz respectively. The spikes in the spectra due to the echo from the satellite are seen more prominently in the spectra having a resolution of 0.49 Hz.

bandwidth (*B*) (or Doppler broadening) of the received echo is:

$$B = \frac{4\pi D}{\lambda P} cos\delta, \tag{1}$$

where λ is the radar wavelength, and δ is the sub-radar latitude[2].

For delay-Doppler imaging, the transmitted signal was modulated by a repeating pseudo-random code using binary phase coding. The received signal was demodulated, sampled, and decoded by cross correlating with a replica of the transmitted code, which yielded a delay resolution equal to the baud length, which is the time length of each symbol of the transmitted code. Rows corresponding to the same time delay in consecutive codes were Fourier transformed to obtain the received signal power as a function of Doppler frequency. The result is a two-dimensional array of radar echo power as a function of time delay and Doppler frequency. Table 1 summarizes our radar observations.

We summed all echo power spectra runs obtained on a single day and measured the echo power in each polarization on each day. The ratio of the power SC/OC gives the circular polarization ratio, denoted by μ_c, which has historically been treated as a zeroth-order gauge of near-surface roughness at decimeter spatial scales (Ostro, 1993). We used data reduction techniques that are well-established and were described in detail by Magri et al. (2007) to compute the radar cross-section (σ) of the target (primary + secondary) in each polarization. The radar cross-section divided by the projected area gives the radar albedo ($\hat{\sigma}$). The uncertainties assigned on the cross-sections and albedos take into consideration systematic pointing and calibration errors, as well as the uncertainty in the target's projected area. In the SC/OC ratios, errors such as pointing and target cross-section largely cancel resulting in

smaller uncertainties.

The Goldstone and Arecibo echo power spectra are shown in Figs. 1 and 2. At the time of the observations, the Goldstone echo power spectra were processed with a frequency resolution of 0.98 Hz. Adopting a threshold of three standard deviations for determining the edges of the echo, we measured a bandwidth of about 30 Hz. The spectra are asymmetric and appear stronger toward positive frequencies because the signal from the satellite overlaps that from the primary. The 1-Hz resolution is too coarse to show the signature of the satellite, which appears as a strong, narrow spike in data processed later at higher frequency resolutions (Fig. 1, right column). The presence of the satellite was unknown during the Goldstone observations because there was no obvious narrow spike in the echo power spectra at 1-Hz resolution as originally processed. The satellite was discovered in lightcurve data (Pravec et al., 2003) after the Goldstone observations and shortly before the Arecibo observations started. Echo power spectra obtained later at Arecibo (Fig. 2) show a narrow, strong spike at about +3 Hz on all three days. After discovery, the Goldstone spectra were reprocessed with 0.49 Hz resolution, which revealed the signal from the satellite (see the right panels of Fig. 1). The echo from the satellite is much narrower than the echo from the primary because the satellite is significantly smaller and because its rotation period is considerably slower. At 0.49 Hz resolution, nearly all the echo power appears in only one Doppler bin, so the echo appears bright relative to the echo from the primary, which is spread out in Doppler frequency due to its rapid rotation and larger diameter. The ratio of primary to secondary bandwidths is similar to that of other binary NEAs (e.g., Margot et al., 2002).

The echo bandwidth in the Arecibo spectra (Fig. 2) is about 9.5 to 10 Hz, which is equivalent to 34 to 36 Hz at X-band. The modestly wider X-band equivalent bandwidth at Arecibo suggests that the sub-radar latitude was closer to the equator during the Arecibo observations, which was later confirmed by shape modeling (Section 4 and Fig. 13).

---

[2] The sub-observer latitude is the latitude of the asteroid surface intercept of the line containing the observer and the target's center.
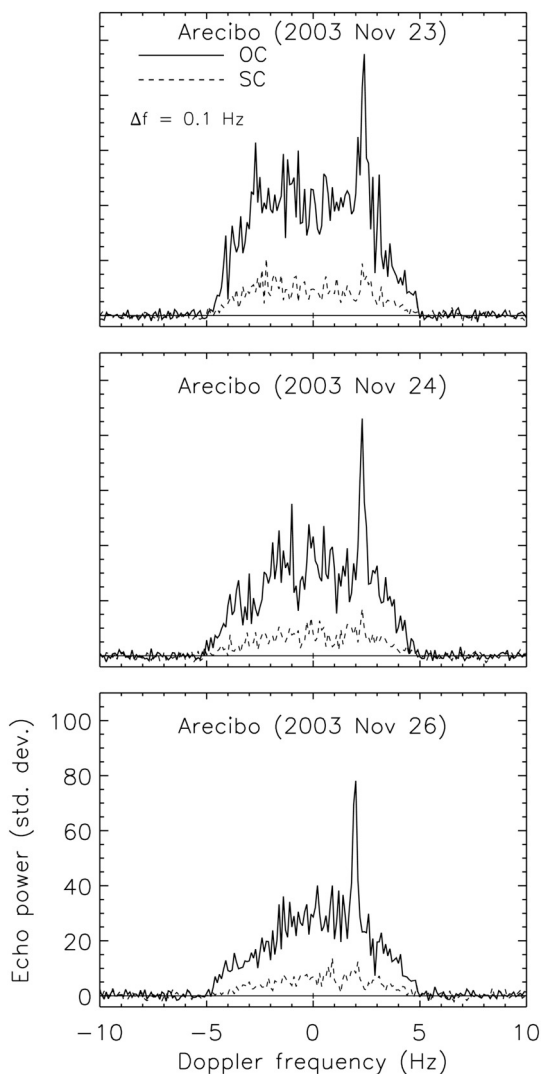
Fig. 2. Single-day sums of echo power spectra obtained at Arecibo. OC and SC spectra are shown using solid and dashed lines respectively. The narrow spike toward the right is the echo from the secondary.

Figs. 3, 4, 5, and 6 show Goldstone and Arecibo delay-Doppler images obtained on November 14, 15, 23, 24, and 26. The finest time delay resolutions obtained at Goldstone and Arecibo were 0.5 μs and 0.1 μs respectively, corresponding to range resolutions of 75 m and 15 m. The finest resolution Goldstone images on November 14 and 15 span about 110 and 640 degrees of primary rotation with some gaps in the coverage (Fig. 3, Table 1). The finest resolution Arecibo images covered 250, 300, and 350 degrees of primary rotation (Figs. 4, 5, and 6). Together the Arecibo radar images with a range resolution of 15 m covered all rotational phases of the primary.

Figs. 7 and 8 show single day weighted sums of all delay-Doppler runs obtained on November 15 at Goldstone, and on November 23, 24, and 26 at Arecibo. The primary's maximum visible range extent using a 2σ noise threshold in the Arecibo images is about 25 rows, corresponding to 375 m at the 15-m/pixel resolution. If we assume that only one hemisphere of the primary was illuminated in any given image, which would be true for a sphere, then this range extent corresponds to a diameter of about twice as large (~750 m).

The unsummed Arecibo images shown in Figs. 4, 5, and 6 show very little variation in the visible range extent of the primary on any given day (<75 m), suggesting that the primary's equatorial dimensions do not vary substantially. However, the leading edge is not circular and multiple flat features are visible in the Arecibo images on all three days.

Brightness variations, most likely due to surface topography, are visible behind the leading edge. For example, in Fig. 4 (top row, second and third images from the left) the dark features behind the leading edge that are surrounded by relatively brighter pixels are probably signatures of a concavity. The images show a relatively strong echo behind the leading edge similar to the power profile displayed by asteroid 341843 (2008 EV5) (Fig. 6 in Busch et al., 2011), which suggests that the primary has an equatorial ridge.

Given that recent spacecraft observations of asteroids 101955 Bennu and 162173 Ryugu show surfaces with numerous large boulders exceeding 10 m in diameter (Lauretta et al., 2019; Watanabe et al., 2019), we looked for radar evidence of boulders on Didymos. Decameter-scale boulders appear in delay-Doppler radar images as small clusters of radar-bright pixels and have been seen in radar images of about twenty near-Earth asteroids (Benner et al., 2015) such as Bennu (Nolan et al., 2013), 33342 (1998 WT24) (Busch et al., 2008), 4179 Toutatis, 308635 (2005 YU55), and 2014 HQ124 (Benner et al., 2015). We do not see clusters of radar-bright pixels in the Didymos images, but this does not rule out the presence of boulders because clusters of radar-bright pixels are not usually evident with SNRs and resolutions comparable to those in the Didymos images.

If we assume an equatorial view and a diameter of 750 m, then the S-band bandwidth of 9.5 Hz and Eq. (1) yield a primary spin period of about 2.2 h, which is consistent with the sidereal period of 2.26 h estimated by Pravec et al. (2006). The time interval between which the facets on the leading edge of the primary repeat is also consistent with a period of 2.26 h. For example, the last image in Fig. 4 shows a similar rotational phase to the third image in Fig. 5 (based on the flat region seen on the leading edge). The time interval between the two images is about 22 h and 38 min, which is consistent with 10 full rotations of the primary with a spin period of about 2.26 h.

Figs. 3–8 also show faint streaks of relatively bright pixels that are clearly separated from the primary. These are the echoes from the satellite. These echoes are weak and smeared in time delay and Doppler frequency so we used a more sophisticated technique to estimate the diameter and spin period of the secondary (Section 3). The satellite appears in very similar positions with respect to the primary on each day because we observed the system at roughly 24-hour intervals, which is about twice the period of the mutual orbit.

3. Secondary size and spin

The echo of the secondary is significantly weaker than that of the primary (Figs. 1–8). In the Goldstone images, the satellite is unresolved and barely visible at a range resolution of 75 m. In the Arecibo images the satellite is resolved in both range and Doppler, but the low SNRs and small dimensions of the satellite do not allow us to obtain precise estimates of its range and Doppler extents. The trailing edge of the echo is not symmetric, as would be expected from a spherical object, thus suggesting an elongated and possibly asymmetric shape. Similar delay-Doppler dispersions were seen at much higher SNRs and resolutions for the secondaries of 66391 (1999 KW4) (Ostro et al., 2006) and 185851 (2000 DP107) (Margot et al., 2002; Naidu et al., 2015).

The orbital motion and rotation of the secondary cause its echo to smear in the radar images. Over the time spanned by two runs, the orbital motion of the satellite exceeds the 15 m range resolution of the Arecibo images. Summing more than two runs smears the signal from the secondary in the image (e.g., Fig. 8) but does not significantly improve the SNRs. In order to improve the SNRs, we shifted the images to align the secondary in each image and then summed them. Due to weak SNRs we were not able to measure the center-of-mass (COM) locations precisely so we modeled its motion using visual estimates of the leading edges. The leading edge and the COM of the secondary follow slightly different paths, which would introduce a small but insignificant bias in our measurements. First, we measured the approximate delay and Doppler positions of the leading edges of the secondary in successive
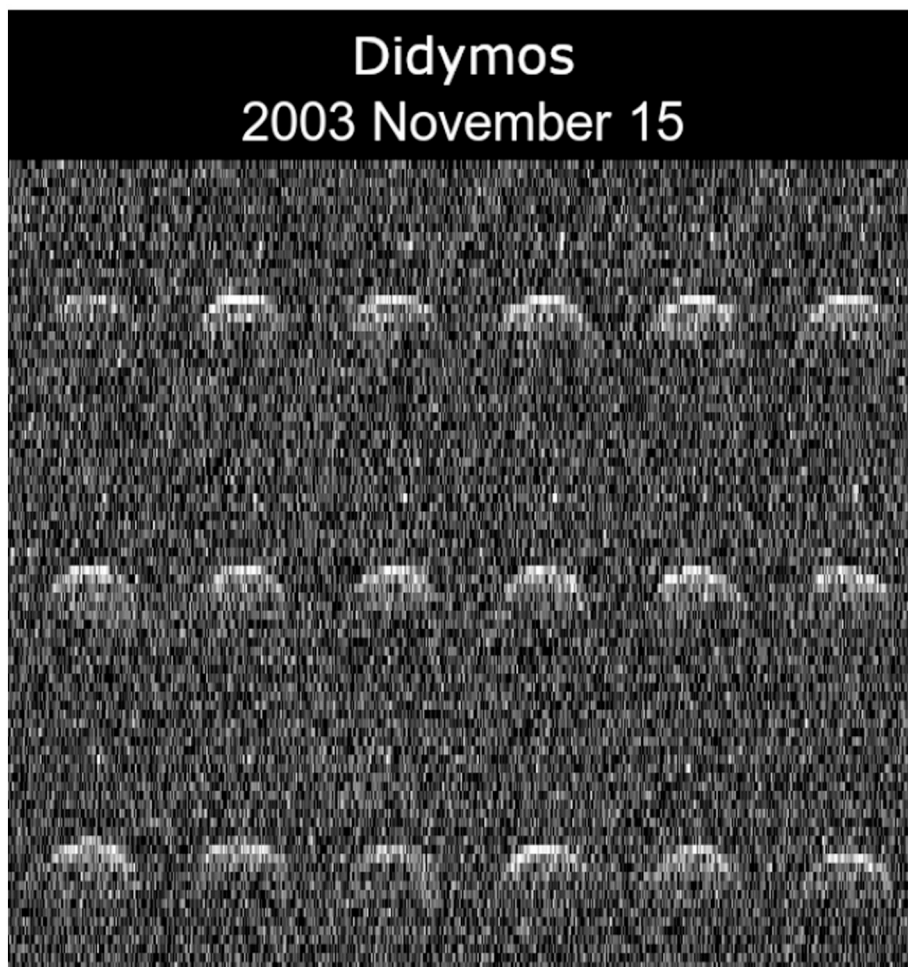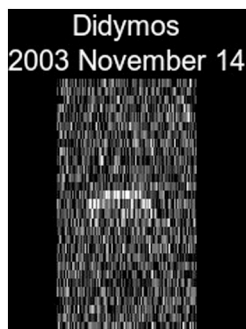
Fig. 3. Goldstone delay-Doppler images of Didymos obtained on 2003 November 14 between 09:05–09:12 UTC (top) and on November 15 between 05:30–09:31 UTC (bottom). The November 14 image is a sum of 4 runs, during which the asteroid rotated about 17°. In the bottom panel, time increases from left to right and top to bottom. Each image is a sum of three runs, during which the primary rotated about 11°. The resolution of the images is 0.5 µs x 0.5 Hz. Within each image, Doppler frequency increases to the right and time delay increases downward. The broad echoes are from the primary and the narrower echoes are from the secondary, whose position changes with time.

Arecibo images. As the satellite orbits the system barycenter its delay and Doppler coordinates follow roughly sinusoidal motion. Using two equations of the form

$$A = P_o + P_1 sin(P_2 t + P_3),$$ (2)

We fit the delay and Doppler positions separately as a function of time. Here A is either the delay or Doppler position, P_o is the delay or Doppler coordinate about which the secondary is orbiting. P_1 and P_2 are the amplitude and angular frequency of the oscillation respectively, and P_3 is the phase of the sinusoid at time $t = 0$. We then shifted the images to align the delay-Doppler coordinates of the satellite in each image according to the estimates obtained from Eq. (2).

This technique allowed us to sum all the images from a single day without any noticeable smear due to the secondary's orbital motion. However, rotational smear is still present, so no information about the rotational variation of the secondary dimensions can be extracted from

the daily summed image. The increased SNRs allowed us to reprocess the images from November 23 and 24 with eight times finer frequency resolution (0.0373 Hz) by using longer Fourier transform lengths. The SNRs on November 26 were too weak to measure the leading edges and apply this technique.

Fig. 9 shows a montage of three frames each from November 23 and 24. Each frame covers about 15 degrees of rotation if we adopt a spin period of 11.9 h. Minor rotational variations on the leading edge are visible in these images and are consistent with the non-zero secondary lightcurve amplitude of 0.02 mag measured by Pravec et al. (2006). However, due to the lack of complete rotational coverage of the secondary and the weak SNRs, we cannot estimate the elongation or the shape of the secondary using the radar data.

Fig. 10 shows daily sums for the satellite echo from November 23 and 24. On both days the visible range extent of the secondary echo, measured using a 2σ noise threshold of contiguous pixels, was about 75
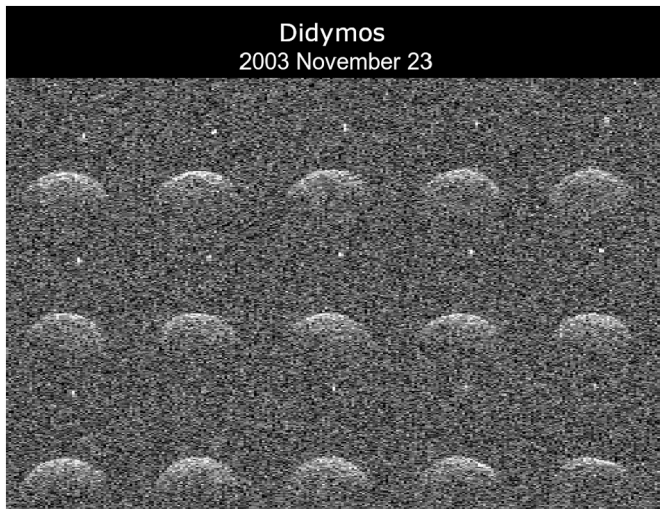
Fig. 4. Arecibo delay-Doppler images of Didymos obtained on 2003 November 23 between 03:24 and 04:58 UTC. Each image is a sum of three runs, during which the primary rotated about 13°. The resolution of the images is 0.1 μs x 0.3 Hz. Delay-Doppler orientations are the same as in Fig. 3.
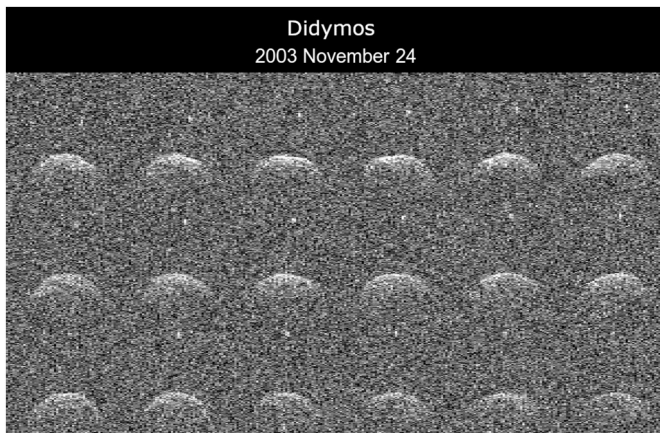

Fig. 6. Arecibo delay-Doppler images of Didymos obtained on 2003 November 26 between 03:08 and 05:20 UTC. Each image is a sum of three runs, during which the primary rotated about 15°. The resolution of the images is 0.1 μs x 0.3 Hz. Delay-Doppler orientations are the same as in Fig. 3.

Fig. 5. Arecibo delay-Doppler images of Didymos obtained on 2003 November 24 between 03:15 and 05:09 UTC. Each image is a sum of three runs, during which the primary rotated about 14°. The resolution of the images is 0.1 μs x 0.3 Hz. Delay-Doppler orientations are the same as in Fig. 3.

m. If we assume that the secondary is roughly spherical, then the diameter would be about double the visible range extent or 150 ± 30 m, where we have assigned a 1σ uncertainty of one pixel in the measured visible extent, which translates to an uncertainty in diameter of 30 m. The diameter estimate is consistent with the value inferred from the secondary-to-primary diameter ratio of 0.22 reported in Pravec et al. (2006) if we adopt the diameter of the primary from the radar shape model. Using the same noise threshold, we measured a bandwidth of 0.34 ± 0.04 Hz for the satellite in both images (the 1σ uncertainty corresponds to 1 Doppler bin). If we use Eq. (1) and assume an equatorial view, then the estimated bandwidth and diameter imply a spin period of 12.4 ± 3.0 h that is consistent with the mutual orbit period of 11.9 h, suggesting that the spin period of the secondary is synchronized to its mutual orbit.

4. Shape and spin state modeling of the primary

We used the SHAPE software (Hudson, 1993; Magri et al., 2007) to fit a spin vector and a shape model to the radar images, echo power spectra, and lightcurves of the primary. The radar data covered five days
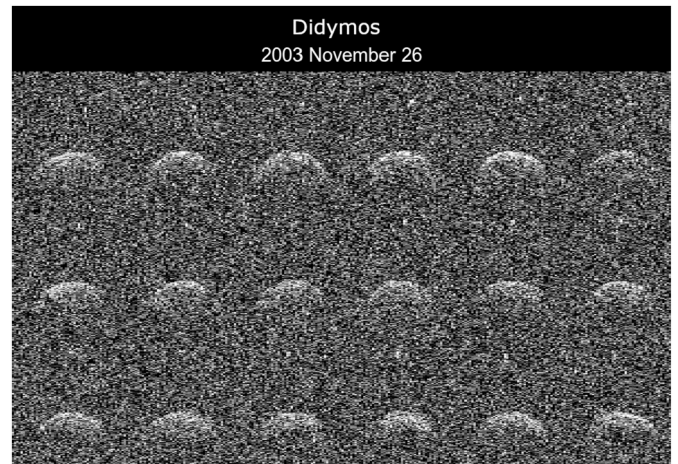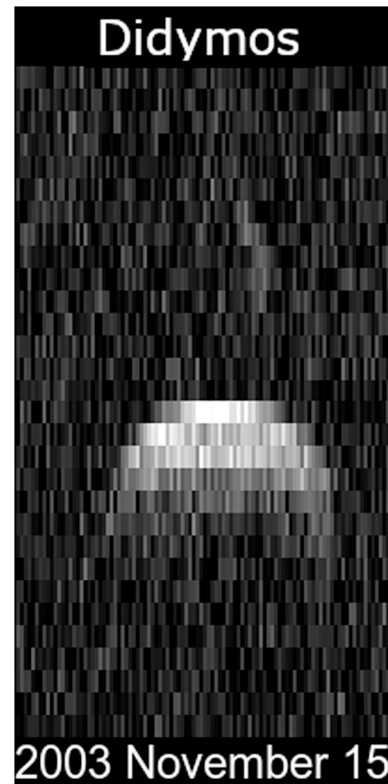

Fig. 7. Single-day sum of delay-Doppler images obtained on Nov 15 at Goldstone. The echo from the satellite is seen as a faint streak above the stronger signal from the primary. The resolution is 0.5 μs x 0.5 Hz.

between November 14 and 26 (Table 1), an interval when Didymos moved about 39° in the sky. Lightcurves were obtained on 16 days between 2003 November 20 and December 20 (Pravec et al., 2006) and cover about 38° of sky motion, and the combined radar and lightcurve dataset cover about 63 degrees of motion. If we assume a spin pole aligned with the binary orbit pole of $(\lambda, \beta) = (310°, -84°)$ (Scheirich and Pravec, 2009), then that implies that the sub-radar latitude moved from about -31 degrees to $-7°$ during the radar campaign. The sub-observer latitude for optical observations moved between -17 degrees to $+9°$.
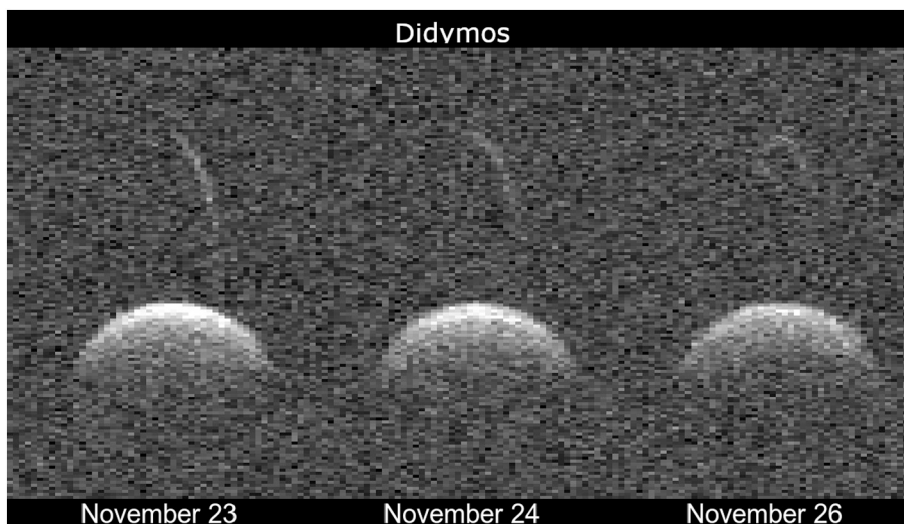
Fig. 8. Single-day sums of delay-Doppler runs obtained using Arecibo. The larger object is the primary and the curved streak is from the secondary whose position changed with time. Image resolutions are 0.1 µs × 0.3 Hz.
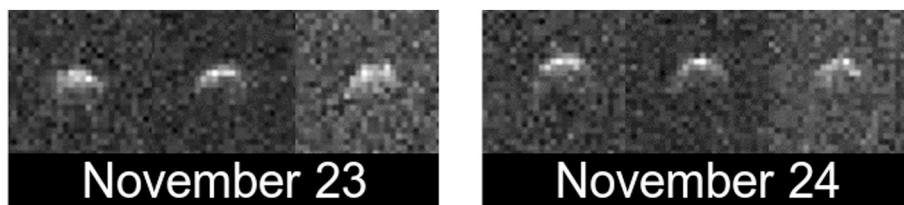

Fig. 9. Satellite delay-Doppler images, each containing sums of about 15 runs. Each frame covers about 15 degrees of rotation by the satellite. The resolution of the images is 0.1 µs x 0.0373 Hz. Subtle asymmetry in the leading edge is visible on both days.
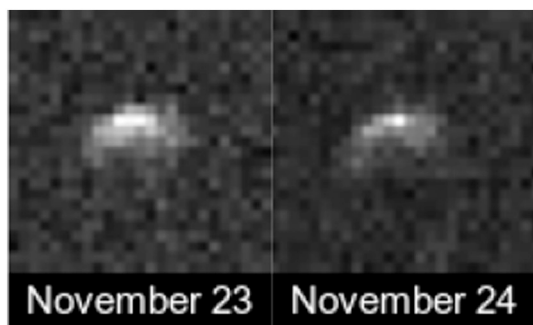

Fig. 10. Single day sums of delay-Doppler images of the satellite obtained using the shift-and-sum technique on November 23 and 24. The resolution of the images is 0.1 µs x 0.0373 Hz.

More lightcurve data was obtained in 2015, 2017, and 2019 (Pravec, private comm.) that we plan to incorporate into a future paper.

The delay-Doppler images and echo power spectra were processed with frequency resolutions listed in Table 1. We summed three runs of data for use in the shape modeling in an attempt to increase the SNRs while limiting rotational smear to <20°. The echo from the satellite was cropped out of the images and frequencies in the echo power spectra containing the satellite echo were set to zero and ignored when computing χ^2. We used all of the lightcurve data from Figs. 1c, 2c, and 3c in Pravec et al. (2006), which include only the contributions from the primary.

We started the modeling with a grid search for the spin axis orientation of the primary. We fit shape models by fixing the spin axis over the entire celestial sphere in increments of 15° in latitude and longitude. For the grid search we fixed the spin period at the nominal sidereal period of 2.26 h (Pravec et al., 2006). Once we obtained our best estimate for the pole direction, we fixed it and then fit for the rotation period and 3D shape. We searched for the rotation period by fixing it at various values and checking the fits, similar to the spin pole search.

We started with triaxial ellipsoids and allowed SHAPE to adjust all three axes to fit the overall shape and size of the object. We then sampled the resulting ellipsoidal shapes using spherical harmonics functions up to degree and order ten to fit the deviations of the shape from a perfect ellipsoid. After obtaining the best fit with a spherical harmonics model, we fit the shape with vertex models that used different numbers of triangular facets in an attempt to fit obvious features in the images while minimizing fitting the noise.

We used a simple Lambertian scattering law having one free parameter (optical albedo) to model optical wavelength scattering from the surface of the asteroid. For the radar data, we used a simple cosine law similar to the one used in Naidu et al. (2015). Imperfections in the knowledge of the asteroid's heliocentric orbit cause the object to drift in range over subsequent delay-Doppler images. SHAPE uses a delay correction polynomial to compensate for drift and to align the synthetic and observed images. We used a second-degree delay correction polynomial and allowed SHAPE to fit the polynomial coefficients.

SHAPE does a sequential fit of the model parameters using a non-linear least squares method that attempts to minimize an objective function that is the sum of χ^2 and a number of penalty functions. χ^2 is computed by comparing a synthetic image, generated from the model, with the observed image. The penalty functions are designed to prevent SHAPE from producing non-physical shapes (Magri et al., 2007). For the grid search (both ellipsoidal and spherical harmonics fits) we used a penalty function to force the body-fixed z-axis to be aligned with the maximum principal moment of inertia of the primary. Fig. 11 shows χ^2
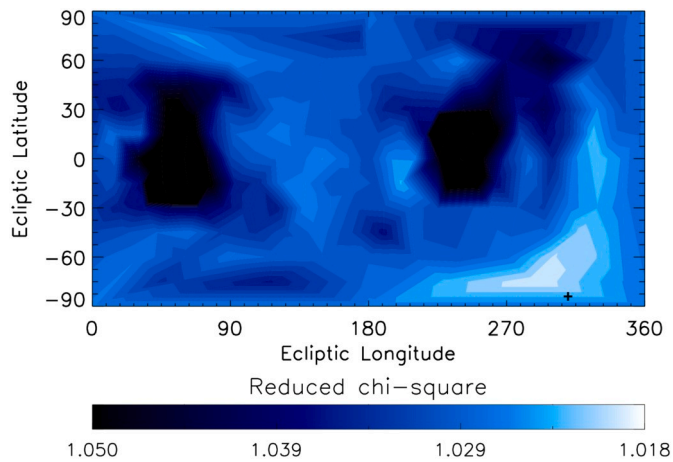
Fig. 11. Contour plot of the goodness of fits (χ^2) of shape models having different spin axis orientations. Models were fit to both radar and lightcurve data. Lighter colors indicate better fits. Plus sign indicates the mutual orbit pole.

for the spherical harmonics shape models as a function of pole direction. A spin pole of $(\lambda, \beta) = (290°, -75°)$ yielded the best fit.

We refined the search for the spin pole around the best-fit value using a finer grid of possible pole directions. We fit 80 shape models with spin poles within 16 degrees of $(\lambda, \beta) = (290°, -75°)$. The spin poles were located along four concentric circles separated by 4, 8, 12, and 16° from the previous best-fit. The spin pole of $(\lambda, \beta) = (296°, -71°)$ yielded the best shape model fit but all of these spin poles provided similar χ^2 values and comparable fits to the data, suggesting that the 1σ uncertainty in our spin pole estimate is at least 16°. The weak constraints on the spin pole are likely due to the limited sky motion during the radar observations.

The mutual orbit pole of $(\lambda, \beta) = (310°, -84°) \pm 10°$ estimated by Scheirich and Pravec (2009) is about 12° from our best-fit spin pole and is within our estimated uncertainty of 16°. We also fit a shape model with Scheirich and Pravec's pole direction and obtained a shape that

looks nearly identical to our best-fit shape. Therefore, it seems reasonable to assume that the spin and orbit poles are aligned due to the action of tidal forces acting in the system (Peale, 1969), so we adopted the mutual orbit pole of $(\lambda, \beta) = (310°, -84°)$ as our nominal spin pole because it has tighter uncertainties from the lightcurve observations.

After we fixed the pole direction, we used the spherical harmonics shape model to estimate the sidereal spin period of the primary by fixing the period at values between 2.2590 h to 2.2610 h in increments of 0.0001 h to test whether we could refine the spin period measurement further. We did not see a noticeable difference in the fits but the model with a spin period of 2.2600 h had the lowest χ^2.

We sampled the best-fit spherical harmonics model to obtain a shape model with 1000 vertices, 1996 triangular facets, and an effective resolution of ~50 m. We allowed SHAPE to fit the vertex coordinates of the model while holding the spin vector fixed. At this stage we added an additional penalty function to prevent SHAPE from trying to create concavities on the model to fit noise in the images. We kept the penalty weight minimal in order to allow concavities where they are clearly visible in the images.

Fig. 12 shows principal axis views of the final vertex shape model, and Figs. 13, 14, and 15 show fits to the radar and lightcurve data. The model is able to fit the overall delay and Doppler dimensions of the radar data well. The primary is shaped somewhat like a top with a prominent equatorial ridge. One of its most prominent features is a facet with a length of ~350 m on the equatorial ridge that is also conspicuous in the leading edges of the imaging data in panels 17–22 of Fig. 13. Another smaller facet is present roughly 120° in longitude from the first. The rest of the surface appears to be smooth at multi-facet scales (~100 m), but this is probably due to the lack of features in the data caused by relatively low signal-to-noise ratios and resolution, and does not imply that the surface is actually smooth at decameter scales. For example, radar images of 10955 Bennu showed only hints of one or two boulders (Nolan et al., 2013) but they are abundant on its surface (Lauretta et al., 2019).

Most of the lightcurve data points are fit well by the shape model (Fig. 15), but there are outliers, especially toward the later dates. These could be due to a number of factors such as smaller scale surface topography that is not visible in the radar images, non-uniform optical
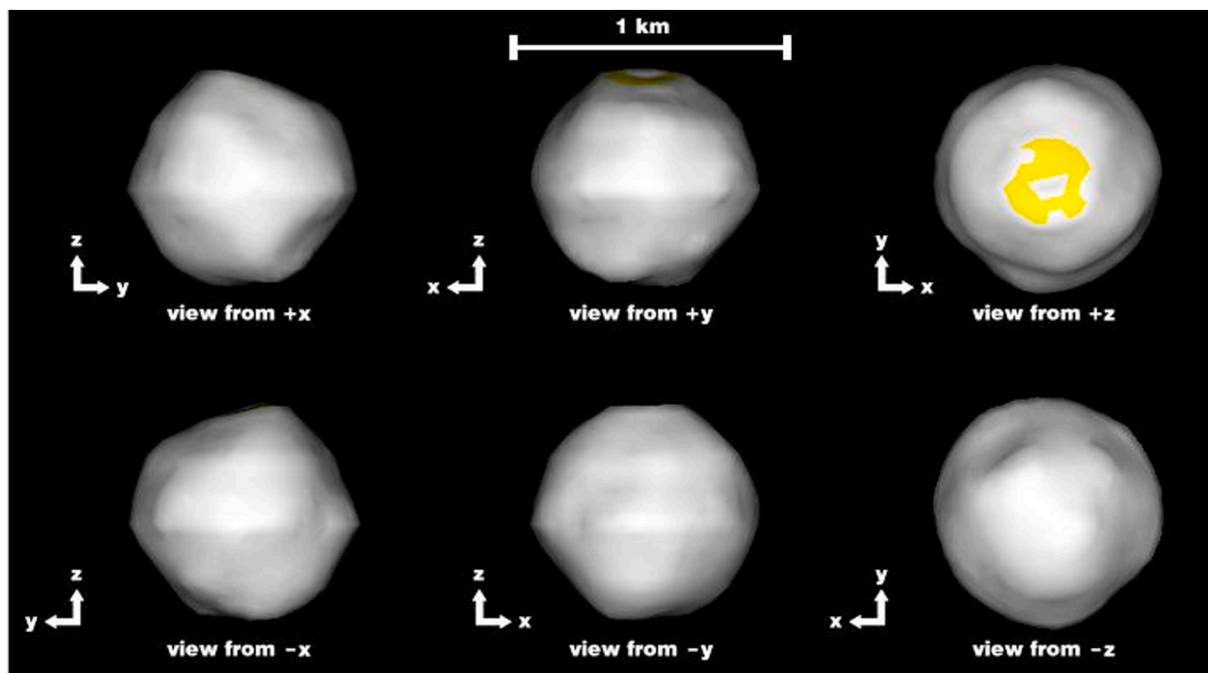

Fig. 12. Principal axis views of the primary shape model. The shape model has 1000 vertices and 1996 triangular facets. The effective resolution of the model is ~50 m. Yellow indicates regions where the incidence and scattering angle are >60°. (For interpretation of the references to colour in this figure legend, the reader is referred to the web version of this article.)
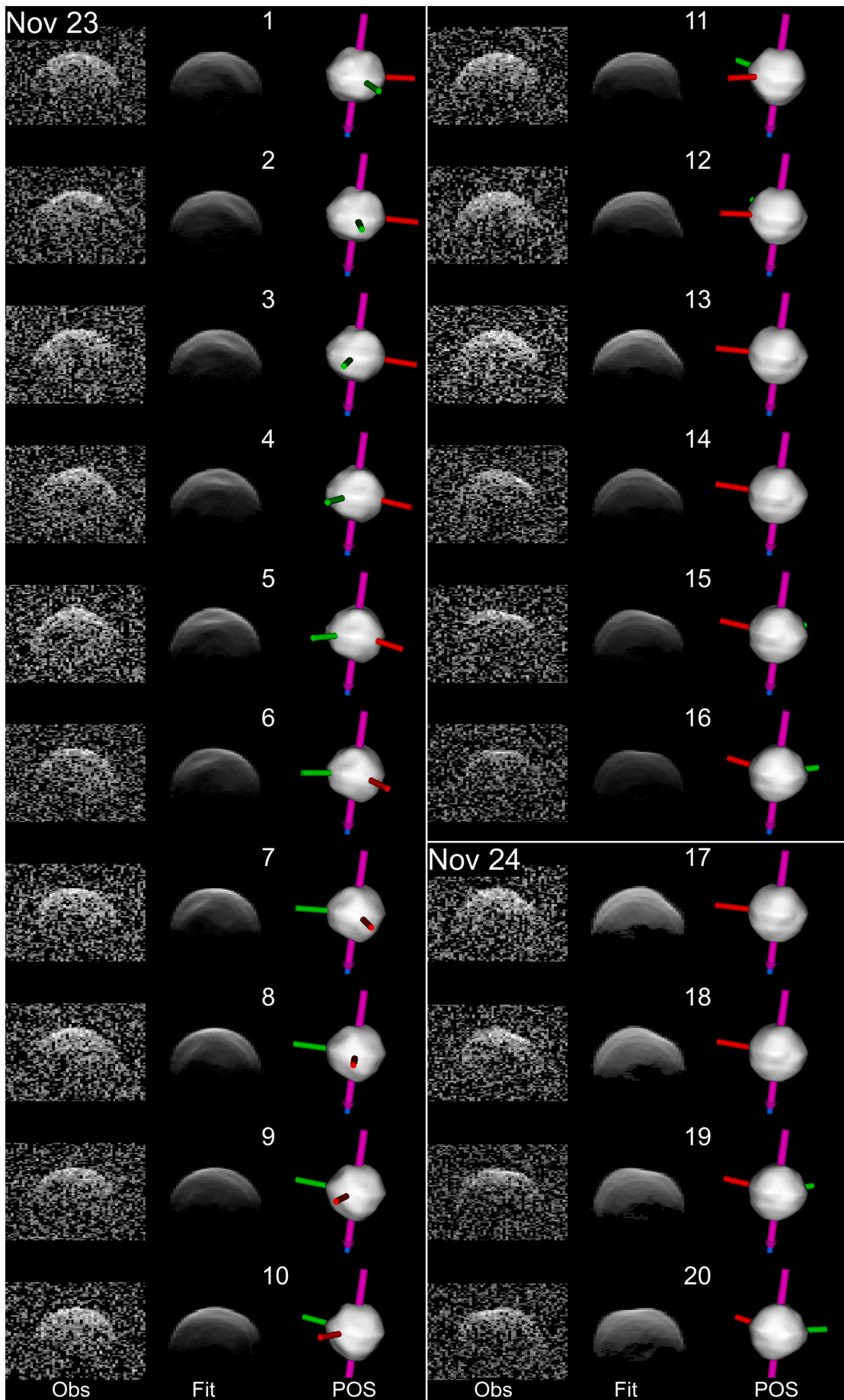
Fig. 13. Shape model fits to radar images. Each row shows the observed image (left), a synthetic image generated from the shape model (center), and the corresponding plane-of-sky (POS) view of the shape model. The red, green, and blue cylinders show the x, y, and z principal axes of the shape model. The blue cylinder is hidden under the pink arrow, which indicates the spin vector. Rows 1 to 53 show Arecibo delay-Doppler images and rows 54 to 76 show Goldstone images. (For interpretation of the references to colour in this figure legend, the reader is referred to the web version of this article.)

◄━━━

scattering over the surface, the simplifying assumptions made by the optical and radar scattering models, and possibly by lack of corresponding radar images at the later dates to constrain features seen in lightcurves.

The nominal shape model shown in Fig. 12 has an equivalent diameter of 780 m. The shape resembles the primary of 276049 (2002 CE26) (Shepard et al., 2006), but with an equatorial ridge similar to ones found on primaries of other binary and triple systems such as 1999 KW4 (Ostro et al., 2006), 311066 (2004 DC) (Taylor, 2009), 136617 (1994 CC) (Brozović et al., 2011), 2000 DP107 (Naidu et al., 2015), as well as on single asteroids such as Ryugu (Watanabe et al., 2019), 2008 EV5 (Busch et al., 2011) and Bennu (Nolan et al., 2013; Lauretta et al., 2019). The equatorial ridge on Didymos is not as prominent as the ridges on the other objects. The properties of the shape model are given in Table 3.

The Dynamically Equivalent Equal Volume Ellipsoid (DEEVE) axes of the model are 783 (± 6%) x 797 (± 6%) x 761 (± 10%) m. The sub-observer latitudes were close to the asteroid's equator throughout the observations so there are regions near the north pole with high radar and optical incidence angles exceeding 60° that we did not see. Consequently, dimensions along the z axis are less well constrained than those along the x and y axes and were assigned a larger 1-sigma uncertainty than along the other two axes.

Given the effective diameter from the 3D model, we compute the optical geometric albedo (p_V) of Didymos by using the relation: (Fowler and Chillemi, 1992; Pravec and Harris, 2007):

$$p_V = \left[\frac{1329 \ km \times 10^{-0.2H}}{D}\right]^2, \tag{3}$$
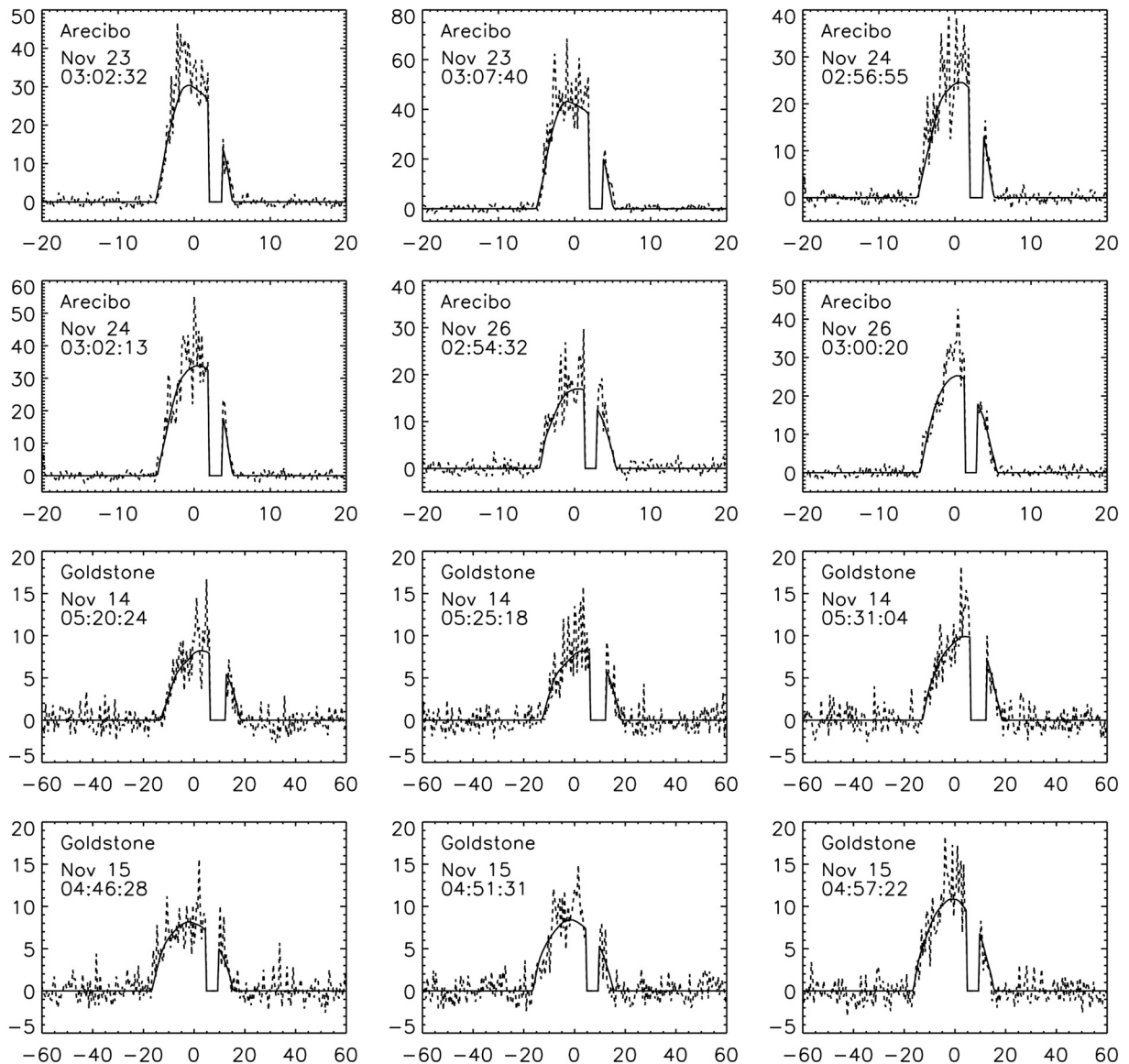

Fig. 14. Shape model fits to OC echo power spectra. The secondary signal was masked out for the primary shape model fit. The frequency resolutions are 0.2 Hz and 0.49 Hz for the Arecibo and Goldstone echo power spectra. Each spectrum is a weighted sum of 2–4 runs. All times are mid-receive UTC.
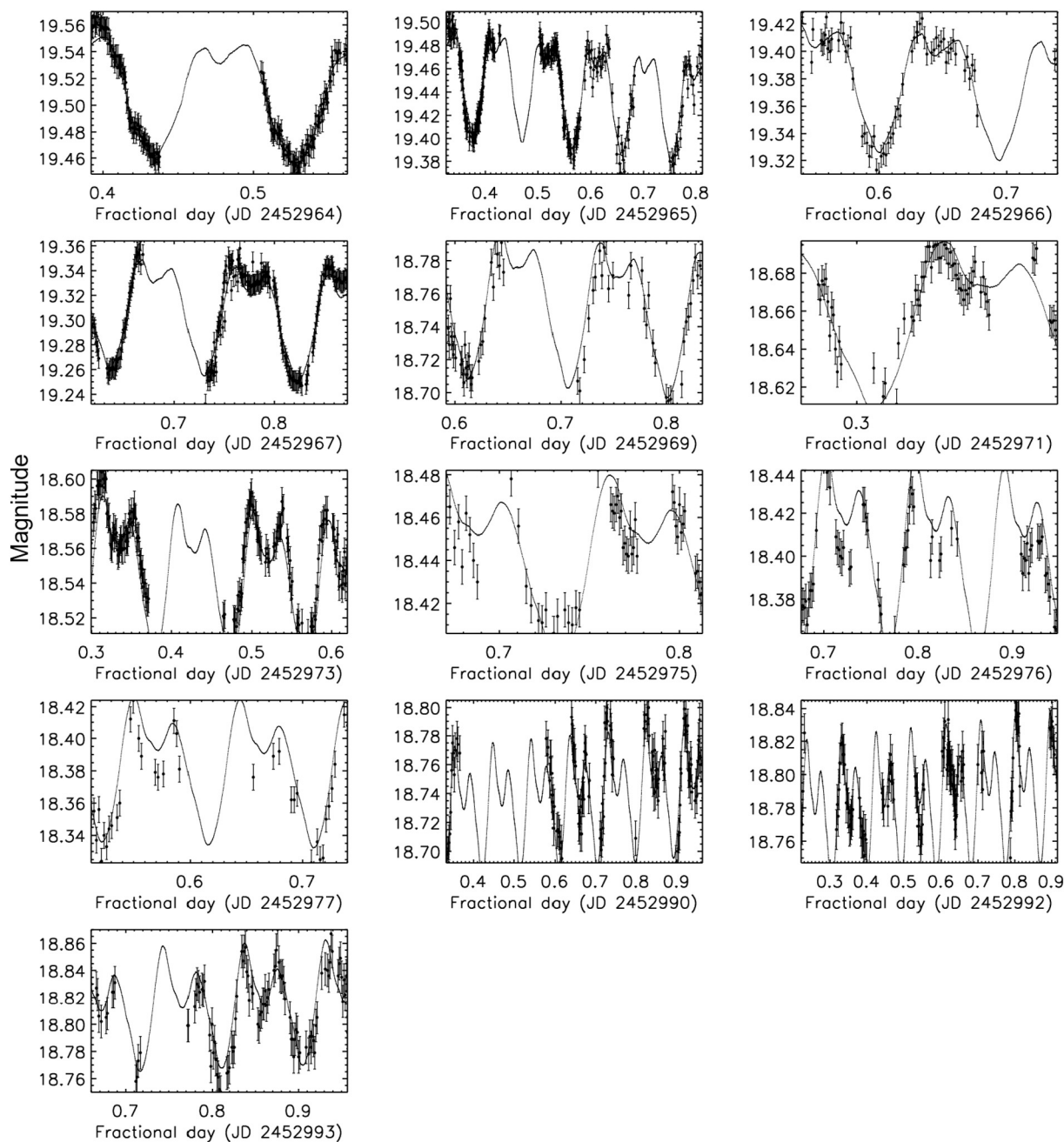
Fig. 15. Shape model fits to lightcurve data from Pravec et al. (2006). The solid line shows the model lightcurves and filled circles show the data points and their uncertainties. All times are one-way light-time corrected Julian Date UTC. Table 2 provides more information about the lightcurve observations.

where D is the diameter of the asteroid, and H is its absolute magnitude. For a binary, D is the effective diameter of the primary and secondary combined, which for Didymos is $\sqrt{D_p^2 + D_s^2}$, where D_p and D_s are the diameters of the primary and secondary. Substituting $D = 794\ m$ and $H = 18.16 \pm 0.04$ (Pravec et al., 2012), we obtain a geometric albedo of 0.15 ± 0.04 that is close to the average value for S-type asteroids.

5. Radar scattering properties

We used the daily weighted sums of echo power spectra to estimate the radar cross-sections, radar albedos, and circular polarization ratios from the Arecibo and Goldstone data (Table 4). The projected areas required for estimating the radar albedos were obtained by using the orientation of the shape model of the primary at the time of the

observations and by assuming that the secondary is a sphere with a diameter of 150 m.

We obtain average daily circular polarization ratios at Arecibo and Goldstone of 0.19–0.21 and 0.22–0.23 respectively, that are consistent within their uncertainties. The average S-band and X-band radar cross sections ($0.099 \pm 0.025\ km^2$ and $0.15 \pm 0.05\ km^2$) and radar albedos (0.2 ± 0.05 and 0.3 ± 0.1) show significantly larger differences but are still consistent within their formal uncertainties. The day-to-day variations in the radar cross section and SC/OC at each observatory are small, but the persistent differences between the average X-band and S-band radar cross sections hint that this difference could be real, which is relatively uncommon among NEAs observed by both telescopes. Such differences could arise due to different surface and near-surface roughness at the two different wavelength scales. The values of μ_c are lower than the average estimated for 214 near-Earth asteroids previously

Table 3

Didymos primary shape model parameters.

Parameters		Values
Extents along principal axes (m)	x	$832 \pm 6\%$
	y	$838 \pm 6\%$
	z	$786 \pm 10\%$
Surface area (m^2)		$1.96 \times 10^6 \pm 8\%$
Volume (m^3)		$2.49 \times 10^8 \pm 12\%$
Principal moments of inertia (kg. m^2)	A	$3.23 \times 10^{16} \pm 13\%$
	B	$3.29 \times 10^{16} \pm 13\%$
	C	$3.38 \times 10^{16} \pm 10\%$
Equivalent diameter (m)		$780 \pm 4\%$
DEEVE extents	x	$797 \pm 6\%$
	y	$783 \pm 6\%$
	z	$761 \pm 10\%$
Spin pole (λ, β)(°)		$(310, -84) \pm 20$
Sidereal spin period (h)		2.2600 ± 0.0001

Note – Surface area was computed as the sum of the area of all the model facets. The moment of inertia values were computed assuming uniform density. A, B, and C, are the principal moments of inertia such that A < B < C. Equivalent diameter is the diameter of a sphere with the same volume as the shape model. The Dynamically Equivalent Equal Volume Ellipsoid (DEEVE) is an ellipsoid with uniform density with the same volume and moments of inertia as the shape model. We assumed that the spin pole is aligned with the mutual orbit pole. All uncertainties are 1σ.

detected by radar, which have a mean of SC/OC = 0.34 ± 0.25 (Benner et al., 2008). The X-band and S-band circular polarization ratios are consistent with previous estimates from the S-class: the mean value for S-type NEAs is 0.27 ± 0.079, computed for 70 asteroids (Benner et al., 2008), and that for S-type main-belt asteroids is 0.198 ± 0.094, computed for 27 asteroids (Magri et al., 2007).

We also estimated the radar albedo and circular polarization ratio of the secondary using the Arecibo echo power spectra. The Goldstone echoes from the secondary were too weak for obtaining meaningful estimates. We modeled the primary contribution to the echo using a fourth-degree polynomial and subtracted it from the total, resulting in a signal containing only the contribution from the secondary. The residual contribution from the primary that might remain has been factored into our uncertainties. The secondary echo power spectra yield estimates of OC radar albedo = 0.28 ± 0.1 and SC/OC = 0.12 ± 0.025, when averaged over the three days. The differences in the radar albedo and circular polarization ratio values of the primary and the secondary body hint at different surface and near-surface properties. The circular polarization ratios and radar albedos of the primary and secondary components of 2000 DP107 (Naidu et al., 2015) and 1999 KW4 (Ostro et al., 2006) appear to be more similar than with Didymos. Table 4 summarizes the radar scattering properties for Didymos and Table 5 compares these results with those obtained for other spacecraft targets also observed by radar.

The handedness of a circularly polarized electromagnetic (EM) wave is reversed upon normal reflection from a dielectric surface whose size and radius of curvature is much greater than the wavelength (Ostro, 1993). The polarization ratio μ_c for such a reflection would be close to zero. Wavelength-scale curvature and multiple reflections result in some

power being returned in the SC polarization and a non-zero value of μ_c. Large circular polarization ratios imply a rougher surface although other factors such as surface electrical properties play a role (Ostro, 1993; Virkki and Muinonen, 2016). Historically, papers on radar characterization of asteroids have used this interpretation to infer that larger values of μ_c indicate greater surface and near-surface roughness. Nolan et al. (2013) reported that asteroid Bennu's circular polarization ratio is 0.18 ± 0.03, which is lower than the values for other near-Earth asteroids visited by spacecraft (Table 5). However, recent OSIRIS-REx spacecraft observations of Bennu (Lauretta et al., 2019) show that its surface is much rougher at decimeter spatial scales than the surfaces of Itokawa, Eros, and Toutatis (Saito et al., 2006; Veverka et al., 1999; Huang et al., 2013), which have somewhat larger circular polarization ratios. This apparent discrepancy implies that factors such as the target's electrical properties, which might have a dependence on the asteroid's spectral class, might play a greater role than surface roughness in determining the value of μ_c. The differences in μ_c values and apparent surface roughness may be in part related to roughness below the surface, which is not observed in spacecraft images. Consequently, SC/OC for Didymos, which is comparable to that of Bennu, may or may not imply a near-surface with similar decimeter-scale roughness. Observations by DART, LICIA cube, Hera, and radar observations of asteroid Ryugu in 2020 will increase the number of spacecraft targets with known radar scattering properties and should improve interpretations of circular polarization ratios.

6. Satellite orbit estimation

We used a weighted least-squares procedure to fit Keplerian orbits to the delay and Doppler positions of the secondary COM with respect to the COM of the primary. As initial conditions, we used the nominal orbital parameters from Michel et al. (2016) but we also explored a grid of orbital elements around their results to check for better solutions. Because of their longer time-baseline, results from lightcurves helped considerably in our search. We used the shape model to locate the COM of the primary under the assumption of uniform density. The SHAPE software aligns the synthetic radar images and echo power spectra, which are derived from the shape model, with the observed data and outputs the coordinates of the COM in the data. We used these primary

Table 5

Radar scattering properties for near-Earth asteroid mission targets.

Object	OC radar albedo		SC/OC	
	Goldstone	Arecibo	Goldstone	Arecibo
433 Eros		0.25 ± 0.09	0.33 ± 0.05	0.28 ± 0.06
4179 Toutatis	0.24 ± 0.03	0.21 ± 0.03	0.29 ± 0.01	0.23 ± 0.03
25143 Itokawa		0.14 ± 0.04	0.47 ± 0.04	0.26 ± 0.04
65803 Didymos	0.30 ± 0.08	0.20 ± 0.05	0.20 ± 0.04	0.22 ± 0.04
101955 Bennu	0.12 ± 0.04	0.12 ± 0.04	0.19 ± 0.03	0.18 ± 0.03

Note – Values for Didymos are averaged over all days at each observatory. Remaining values are taken from Table 3 in Nolan et al., 2013 and references therein.

Table 4

Disk-integrated radar properties.

Date	Frequency Band	σ_{oc} (km^2)	$\hat{\sigma}_{oc}$	μ_c	Secondary σ_{oc} (km^2)	Secondary $\hat{\sigma}_{oc}$	Secondary μ_c
Nov 14	X	0.144 ± 0.05	0.29 ± 0.1	0.21 ± 0.02			
Nov 15	X	0.154 ± 0.05	0.31 ± 0.1	0.19 ± 0.02			
Nov 23	S	0.099 ± 0.025	0.20 ± 0.05	0.22 ± 0.02	0.0056 ± 0.0022	0.28 ± 0.11	0.11 ± 0.02
Nov 24	S	0.099 ± 0.025	0.20 ± 0.05	0.22 ± 0.02	0.0050 ± 0.002	0.25 ± 0.10	0.12 ± 0.02
Nov 26	S	0.099 ± 0.025	0.19 ± 0.05	0.23 ± 0.02	0.0062 ± 0.0025	0.31 ± 0.12	0.14 ± 0.03

Note - σ_{oc} is the OC radar cross-section and $\hat{\sigma}_{oc}$ is the OC radar albedo. X- and S-band correspond to the carrier frequencies at Goldstone (8560 MHz) and Arecibo (2380 MHz). The values in the third, fourth, and fifth columns were measured for the whole system, whereas the values in the last three columns were measured for the satellite after modeling and removing the contribution to the echo from the primary. The secondary was assumed to be a sphere with a radius of 80 m.

Table 6

Estimates of delay and Doppler separations between secondary and primary centers-of-mass (COM) in the delay-Doppler images.

Date YYYY MM DD.DDDDD (UTC)	Range separation (m)	Range separation Uncertainty (m)	Doppler separation (Hz)	Doppler separation uncertainty (Hz)	Obs.
2003 11 14.38123	−620	300	−7.09	2.0	G
2003 11 15.23426	−805	300	5.56	2.0	G
2003 11 15.23774	−861	300	5.56	2.0	G
2003 11 15.24125	−879	300	5.07	2.0	G
2003 11 15.24473	−897	300	4.57	2.0	G
2003 11 15.24823	−968	300	4.08	2.0	G
2003 11 15.25171	−956	300	3.83	2.0	G
2003 11 15.25520	−952	300	3.58	2.0	G
2003 11 15.25868	−970	300	3.08	2.0	G
2003 11 15.26216	−973	300	2.84	2.0	G
2003 11 15.26567	−1028	300	2.84	2.0	G
2003 11 15.26917	−1069	300	2.34	2.0	G
2003 11 15.27266	−1065	300	1.85	2.0	G
2003 11 15.27558	−1045	300	2.09	2.0	G
2003 11 15.31603	−998	300	−2.62	2.0	G
2003 11 23.14338	−776	60	1.81	1.2	A
2003 11 23.14762	−818	60	1.71	1.2	A
2003 11 23.15185	−873	60	1.52	1.2	A
2003 11 23.15609	−908	60	1.52	1.2	A
2003 11 23.16032	−942	60	1.36	1.2	A
2003 11 23.16456	−991	60	1.20	1.2	A
2003 11 23.16880	−1018	60	1.17	1.2	A
2003 11 23.17303	−1052	60	0.91	1.2	A
2003 11 23.17727	−1071	60	0.93	1.2	A
2003 11 23.18150	−1084	60	0.68	1.2	A
2003 11 23.18574	−1103	60	0.62	1.2	A
2003 11 23.19421	−1149	60	0.28	1.2	A
2003 11 23.20269	−1180	60	−0.03	1.2	A
2003 11 24.14163	−851	60	1.60	1.2	A
2003 11 24.14601	−900	60	1.59	1.2	A
2003 11 24.15038	−942	60	1.51	1.2	A
2003 11 24.15922	−1011	60	1.19	1.2	A
2003 11 24.16811	−1094	60	0.89	1.2	A
2003 11 24.17256	−1113	60	0.78	1.2	A
2003 11 24.17700	−1140	60	0.72	1.2	A
2003 11 24.18589	−1157	60	0.30	1.2	A
2003 11 24.19478	−1180	60	−0.08	1.2	A
2003 11 24.19922	−1191	60	−0.16	1.2	A
2003 11 24.20367	−1210	60	−0.33	1.2	A
2003 11 26.13231	−933	60	1.53	1.2	A
2003 11 26.13711	−979	60	1.33	1.2	A
2003 11 26.14190	−1016	60	1.17	1.2	A
2003 11 26.14669	−1043	60	1.07	1.2	A
2003 11 26.15148	−1090	60	0.91	1.2	A
2003 11 26.16106	−1159	60	0.63	1.2	A
2003 11 26.17544	−1188	60	0.02	1.2	A
2003 11 26.18502	−1195	60	−0.27	1.2	A
2003 11 26.20419	−1185	60	−0.88	1.2	A

Note—Range and Doppler separations are the secondary COM minus the primary COM. In the final column, A and G refer to Arecibo and Goldstone. Section 6 explains the method used to obtain these measurements.

COM locations for the orbit estimation.

Since we do not have a shape model for the secondary, we assumed that the secondary COM occurs on the trailing edge echoes in the images and at the center of the secondary spike in the echo power spectra. This is a good approximation if the secondary has a triaxial ellipsoid shape and a uniform density. We assigned uncertainties of 4 rows and columns to both the delay and Doppler separation measurements, corresponding to uncertainties of 60 m and 1.2–2 Hz. Tables 6 and 7 show the 108 delay and Doppler separation measurements and their uncertainties that were used for the fit, and Fig. 16 shows the residuals. Because these range-Doppler measurements are based on a detailed 3D model of the primary, they are more precise than the visual estimates used by Fang and Margot (2012).

The best-fit orbit has a semimajor axis a = 1190 ± 30 m, eccentricity e < 0.05, period P = 11.93 ± 0.01 h, and a system mass M_{sys} = (5.4 ± 0.4) x 10^{11} kg. The orbit pole is at (λ, β) = (290°, −89°) ± 10°, which is about 5° from the value of (λ, β) = (310°, −84°) estimated by Pravec and Scheirich (2018). The orbital elements are also consistent with the

values estimated by Fang and Margot (2012).

If we assume that the primary and secondary have equal densities, then based on their size estimates from sections 3 and 4, the secondary contains <1% of the system mass, so we can assume that the primary mass is roughly equal to the system mass. We divided the system mass by the volume of the primary and estimated a bulk density of 2170 kg m^{-3} ± 15%. Table 8 compares this value with densities of several other near-Earth objects. If we assume a grain density of 3700 kg m^{-3}, which is typical for an ordinary chondrite meteorite analog (eg., Ostro et al., 2006), then we estimate a porosity of about 40%. Under the assumption of equal density, the mass of the secondary is about 3.8 × 10^9 kg, which is <1% of the mass of the primary. The mass of the secondary would generate a reflex motion by the primary of about 10 m around the system barycenter, which is less than the finest range-resolution of the Arecibo images, making it undetectable in the radar dataset. Due to the lack of reflex motion in the observations, we are not able to obtain an independent estimate of the mass of the secondary. Reflex motion has been detected in radar observations of other binary systems, such as

13

Table 7

Estimates of Doppler separations between secondary and primary COMs in the echo power spectra.

Date YYYY MM DD. DDDDD (UTC)	Doppler separation (Hz)	Doppler separation Uncertainty (Hz)	Obs.
2003 11 14.22250	6.92	2.0	G
2003 11 14.22590	6.92	2.0	G
2003 11 14.22991	6.52	2.0	G
2003 11 15.19894	7.61	2.0	G
2003 11 15.20244	7.61	2.0	G
2003 11 15.20650	7.61	2.0	G
2003 11 23.12676	2.58	0.8	A
2003 11 23.13032	2.58	0.8	A
2003 11 24.12286	2.33	0.8	A
2003 11 24.12654	2.13	0.8	A
2003 11 26.12120	1.82	0.8	A
2003 11 26.12523	1.82	0.8	A

Note—Doppler separations are the secondary COM minus the primary COM. Notation is the same as in Table 6. Section 6 explains the method used to obtain these measurements.
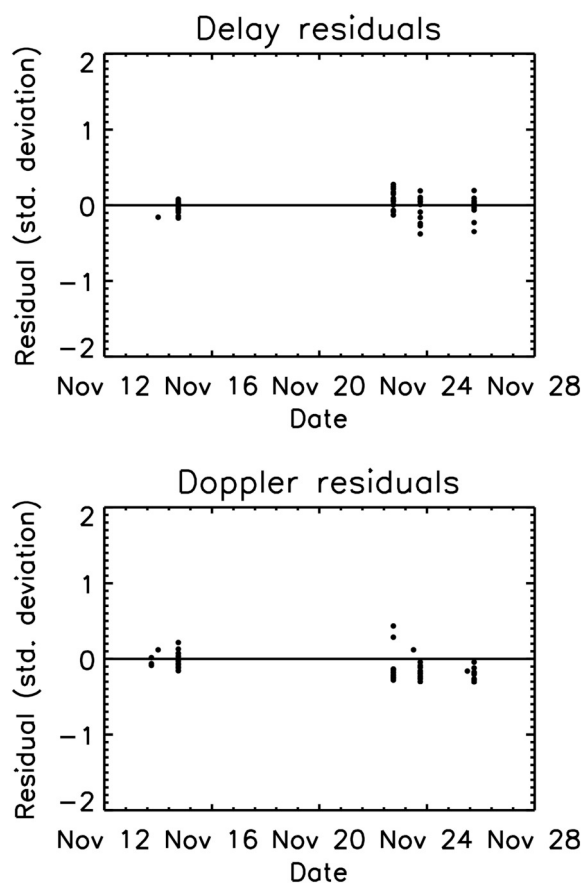

Fig. 16. Delay (top) and Doppler (bottom) residuals of the best-fit mutual orbit normalized by the weight of the measurements.

2000 DP107 (Margot et al., 2002; Naidu et al., 2015) and 1999 KW4 (Ostro et al., 2006).

7. Size and spin limits on additional satellites

Other than the primary and secondary, no other echoes are visible in the radar data. The SNR of an object can be maximized by matching the frequency resolution of the data with the bandwidth of the echo, but

Table 8

Bulk densities estimated for selected near-Earth objects.

Asteroid	Density (kg m^{-3})	Reference
433 Eros	2670 ± 30	Yeomans et al., 2000
6489 Golevka	$2700 + 400/-600$	Chesley et al., 2003
25143 Itokawa	1900 ± 130	Fujiwara et al., 2006
65803 Didymos (system)	2170 ± 350	This paper
66391 (1999 KW4) (primary)	1970 ± 240	Ostro et al., 2006
66391 (1999 KW4) (secondary)	$2810 + 0.82/-0.63$	Ostro et al., 2006
101955 Bennu	1190 ± 13	Lauretta et al., 2019
136617 (1994 CC) (system)	2100 ± 600	Brozović et al., 2011
153591 (2001 SN263) (primary)	1100 ± 200	Becker et al., 2015
162173 Ryugu	1190 ± 20	Watanabe et al., 2019
185851 (2000 DP107) (primary)	1380 ± 250	Naidu et al., 2015
185851 (2000 DP107) (secondary)	1050 ± 250	Naidu et al., 2015
276049 (2002 CE26)	$900 + 500/-400$	Shepard et al., 2006

because we do not know the bandwidth of any potential tertiary signal, we searched for it by processing the echo power spectra and delay-Doppler images with different Doppler frequency resolutions. We also tried summing several runs together to increase SNRs of any additional objects and to look for moving pixels. We inspected individual images and also animated them, a technique that has proven effective to detect the delay-Doppler motion of satellites with weak SNRs. Despite all of these searches, we did not find evidence for additional satellites. Nevertheless, we can use the non-detection to place bounds on the diameter and rotation period of any possible companions.

In general, the radar detectability of a target, which is the ratio of the echo power to the root-mean-square statistical fluctuation of the noise power, is directly proportional to the projected cross-section of the target in the plane-of-sky and inversely proportional to the square root of the target's spin period (e.g., Harmon et al., 2004). We assume that any potential companion would be spheroidal and that any echo with a signal-to-noise ratio ≥ 4 would be visible. Eq. (4) in Harmon et al. (2004) provides a means to estimate if an echo from an object will be detectable. Applying the equation and incorporating observational parameters relevant to Didymos, we get $R^3P < 31250$ m^{3}h, where R is the radius of the potential satellite in meters and P is its spin period in hours. This provides a joint constraint on diameters and rotation periods that yield SNRs too weak for us to detect. The faster the spin period of an undetected satellite, the larger its radius can be. For example, a rotation period of $P > 0.3$ h implies R < ~50 m. Faster rotation periods allow larger satellites to remain undetected, but within limits: asteroids larger than about 150 m in diameter rarely have spin periods faster than 2.1 h (Pravec et al., 2002) and all near-Earth asteroid satellites with known spin periods have values greater than 2.1 h (Margot et al., 2015; Pravec et al., 2016). A spin period of 2.1 h provides a constraint that R < 25 m.

8. Gravitational environment

Assuming a uniform density of 2170 kg m^{-3}, we mapped the gravity field on the surface of the primary using the method of Werner and Scheeres (1997). The assumption of uniform density is justified by the small internal density variations observed on other asteroids such as Eros (Yeomans et al., 2000). The acceleration on the surface of the asteroid is given by the sum of the acceleration due to mass and the centrifugal acceleration. Fig. 17 shows the magnitude of the total acceleration. The acceleration varies between 0.23 mm s^{-2} at the poles to close to 0 mm s^{-2} at the equator. The acceleration map forms concentric rings around the spin axis, indicating that centrifugal acceleration makes a significant contribution to the overall gravity field, similar to asteroids 1999 KW4 (Ostro et al., 2006), 2000 DP107 (Naidu et al., 2015), and other top-shaped asteroids.

Fig. 18 shows the corresponding gravitational slopes, i.e., the angles subtended by the local acceleration vector and the corresponding surface normal pointing inwards. The gravitational slopes vary between ~0° at the poles to ~180° at the equator. The high slopes indicate that,
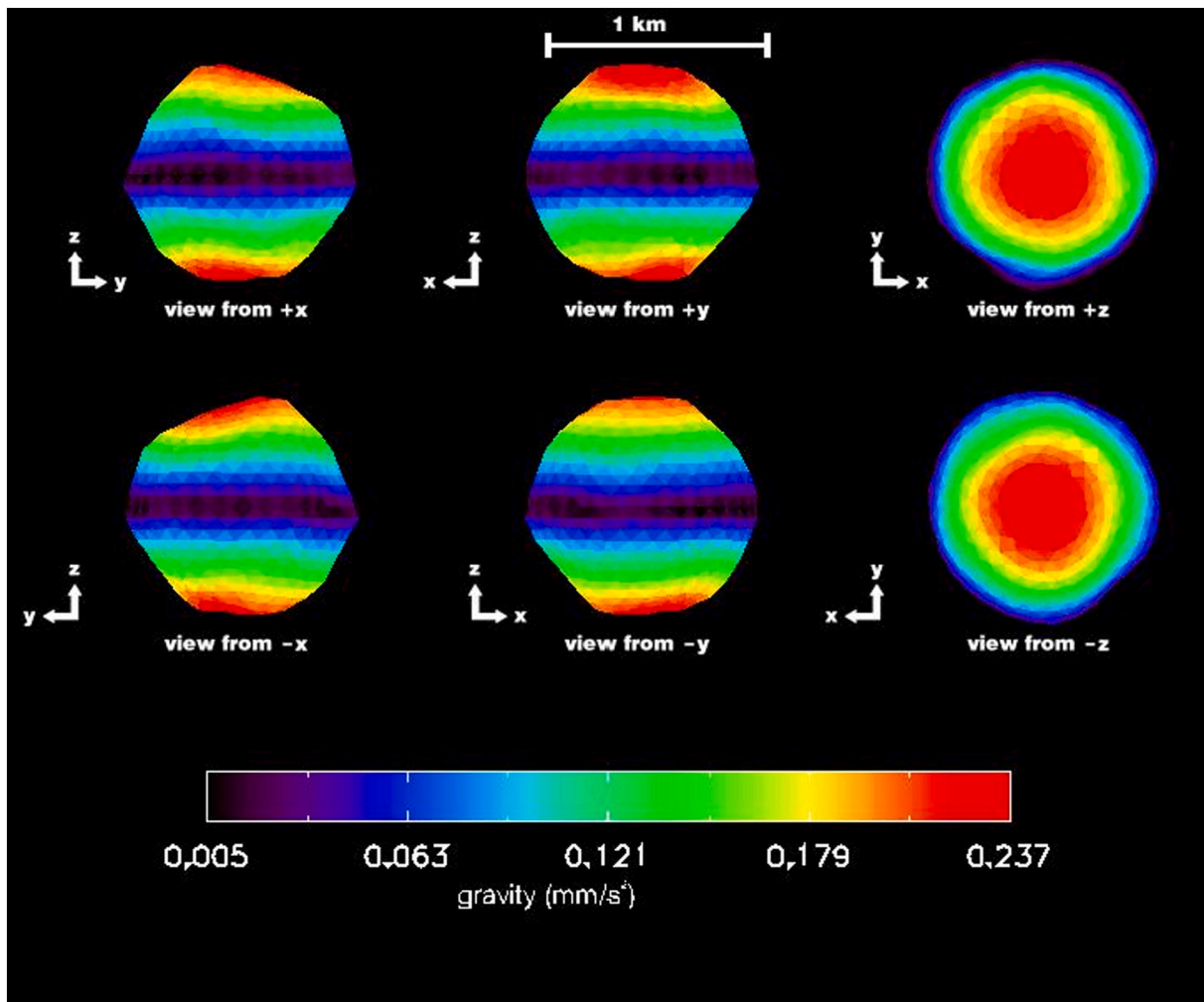
Fig. 17. Magnitude of the vector sum of acceleration due to gravity and centrifugal acceleration. We assumed a uniform density of 2170 kg m^{-3} and a spin period of 2.26 h. Centrifugal acceleration makes a significant contribution to the total acceleration and at the equator it almost cancels out the acceleration due to gravity.

at the equator, the centrifugal acceleration is stronger than the acceleration due to the asteroid's mass. The mid-latitudes mostly have slopes between 45 and 90° that are greater than the angle of repose of most geological materials, which are typically between ~35–45°. This suggests that the surface might lack fine-grained regolith, which tends to have a lower angle of repose. There could also be cohesion that is keeping the surface intact or the density of the asteroid is higher than the nominal value estimated in this paper. Scaling the shape model dimensions down by 5% reduces the slopes almost everywhere on the equator to <90°.

9. Structural analysis and formation of the equatorial ridge

In this section we investigate possible mechanisms for forming the primary's shape and its equatorial ridge, and infer mechanical properties such as its minimum cohesive strength and internal structure. We use a tool called ANSYS Mechanical APDL (version 18.1) to conduct a plastic finite element model (FEM) analysis to study deformation and determine the minimum cohesive strength required to maintain the primary's shape (Hirabayashi and Scheeres, 2014; Hirabayashi et al., 2016; Hirabayashi and Scheeres, 2019). This FEM analysis was first given by Hirabayashi et al. (2017), and detailed analyses were also conducted by Zhang et al. (2017) and Zhang et al. (2018), who employed a Soft-Sphere Discrete-Element Model (SSDEM) technique, confirming consistency with this technique. Our FEM technique consists of a linear elastic mode and a perfect plastic deformation mode that

assumes an associated flow rule (Hirabayashi and Scheeres, 2019). Young's modulus is fixed at 10^7 Pa (Lambe and Whitman, 2008), while Poisson's ratio is defined as 0.25. Failure happens when an element starts experiencing plastic (or irreversible) deformation and is modeled by using the Drucker-Prager yield criterion (Chen and Han, 2007), which is a function of friction angle and cohesive strength. The friction angle is fixed at 35°, which is a typical value for geological materials (Lambe and Whitman, 2008) and cohesive strength is treated as a free parameter to determine the minimum value needed to maintain Didymos' current shape.

We determine the minimum value of cohesive strength that is required to keep the current stress in the body less than or equal to its yield stress. We study the failure modes at two different spin periods: its current spin period of 2.26 h and a longer spin period of 3.5 h, which the Didymos primary might have gone through in the past. These two cases demonstrate different possible failure mechanisms that Didymos may have undergone to attain its current shape. We assume a uniform structure and a bulk density of 2170 kg m^{-3}.

For the 2.26-h spin period case, the failure mode of Didymos should be structural failure in the interior (panels a and b in Fig. 19), which has widely been discussed by earlier works (e.g., Hirabayashi et al., 2017; Zhang et al., 2017; Zhang et al., 2018; Hirabayashi and Scheeres, 2019). The critical deformation mode consists of outward deformation on the equatorial plane and vertical deformation in other regions (panel a in Fig. 19), which is consistent with the failure mode of other spinning top-shaped asteroids (Hirabayashi and Scheeres, 2019). Because of this
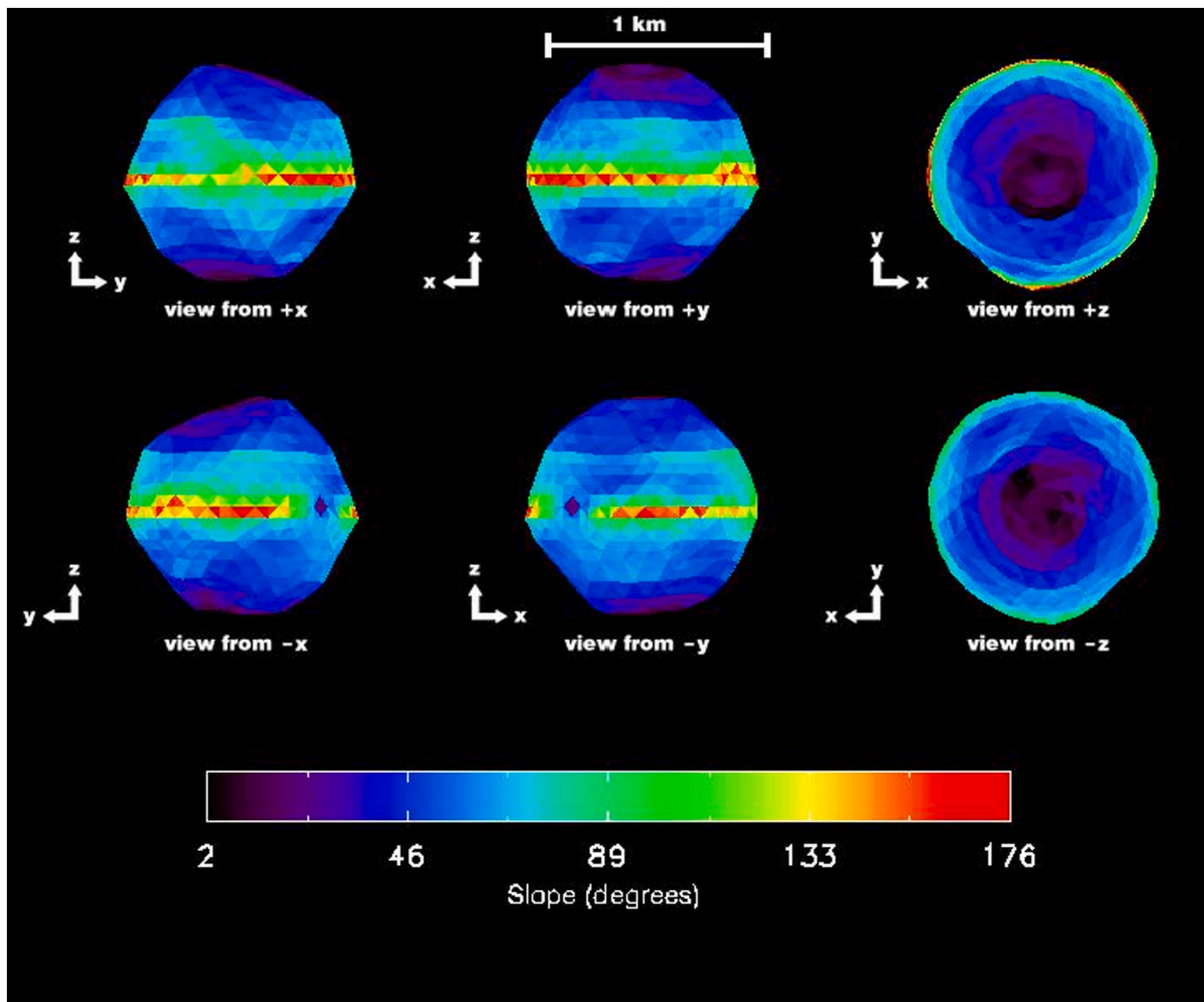
Fig. 18. Gravitational slopes on the surface of the shape model. We assumed a uniform density of 2170 kg m^{-3} and a spin period of 2.26 h. Slopes are close to 0° at the poles and are mostly close to 180° at the equator. Slopes at the mid-latitudes are between 45 and 90°.

failure mode, the surface regions at low latitudes may also experience failure (Fig. 19b). The minimum cohesive strength at this spin period is ~20 Pa, similar to that of Ryugu, which has a value of ~4 and ~ 10 Pa (Watanabe et al., 2019; Hirabayashi et al., 2019).

Contrary to the 2.26-h spin period case, the 3.5-h spin period case shows a different failure mode. Hirabayashi (2015) first predicted that if a spheroidal object that rotates slowly has nearly zero cohesion, then the surface condition becomes more sensitive to failure than the interior. Applying his technique, we find that Didymos should occupy this mode when the spin period is >~2.5 h. Fig. 19c and d show examples of structural failure at a spin period of 3.5 h. Local patches of failure randomly spread over the surface but tend to be located at low latitudes (Fig. 19d) where the gravitational slope is high (Fig. 18). The deformation vectors mainly point toward the center (Fig. 19d). Note that the lengths of the vectors are enhanced to describe the direction of the deformation.

Fast rotation is one of the contributors to the formation of a spinning top-shaped asteroid, and previous work hypothesized that either landslides (Walsh et al., 2008; Minton, 2008; Harris et al., 2009; Walsh et al., 2012) or internal deformation (e.g., Hirabayashi and Scheeres, 2014) may result in the equatorial ridge formation. Importantly, these two different failure modes can be reconciled by considering the internal heterogeneity (Hirabayashi, 2015). As discussed above, if the structure is uniform, then internal deformation may be a primary contributor to ridge formation. If there is a strong core, then the interior can resist against strong loadings, while the surface regions may fail, causing mass

wasting. These scenarios were examined by Zhang et al. (2017, 2018). Also, Hirabayashi (2015) pointed out that even if the spin period does not reach an asteroid's critical spin, thin surface layers may structurally fail (Fig. 19c and d), possibly causing mass movement at a limited level. However, if this process continues for a long period, it may result in the formation of the equatorial ridge.

At present, we cannot rule out these processes as contributors to the formation of the ridge. The DART, LICIACube, and Hera missions could place strong constraints on the formation of equatorial ridges on rapidly spinning asteroids. Specifically, detailed images of the surface morphology of Didymos will determine how deformation occurs in a microgravity environment and provide constraints on the internal structure of this asteroid.

10. Future radar opportunities

Didymos will closely encounter Earth within 0.071 au on October 4, 2022, a few days after the DART impact. During this apparition Didymos will be a moderately strong radar target at Goldstone and an imaging target at Arecibo. Goldstone will be able to observe Didymos before, during, and after the planned DART impact, and Arecibo will be able observe it starting about 24 days after the impact. The Green Bank Telescope (GBT) will be able to receive echoes starting the day after the impact. Estimated Goldstone monostatic, Goldstone-GBT bistatic, and Arecibo radar SNRs and view periods are listed in Tables A1-A4. The SNR calculations assume Arecibo and Goldstone transmitter powers of
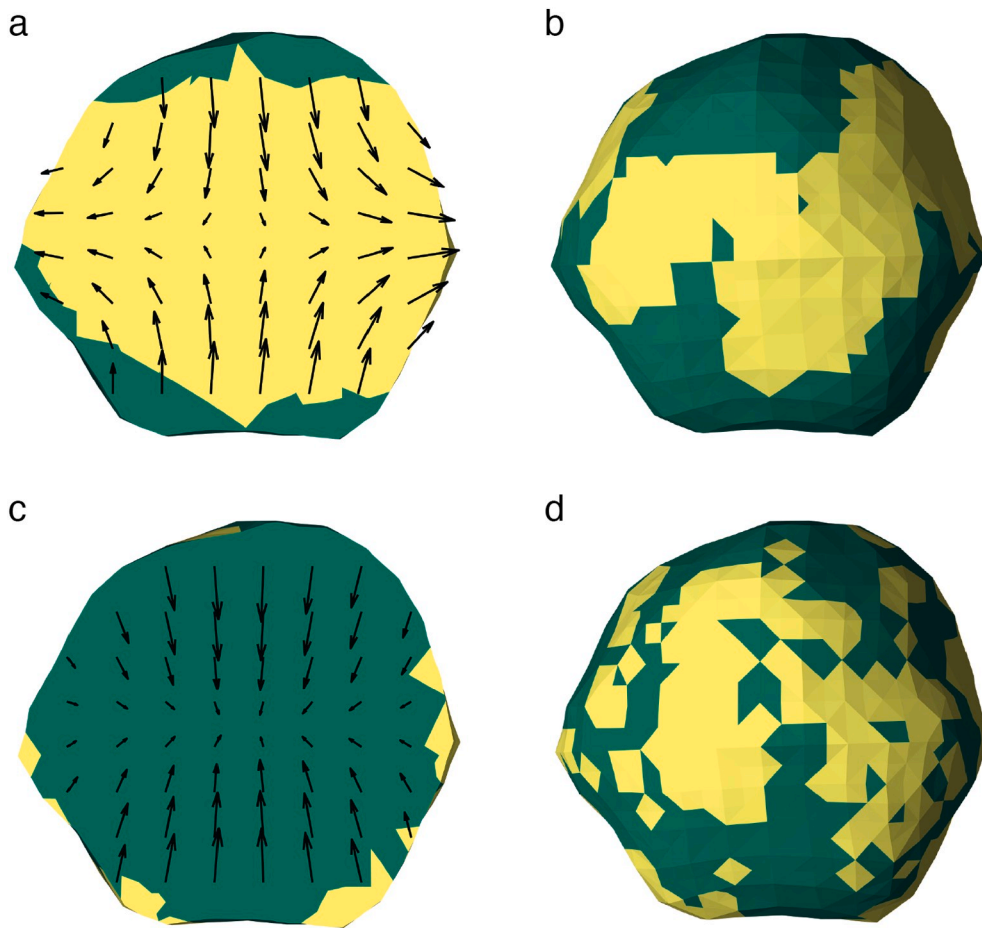
Fig. 19. Stress solutions from the finite element model analysis of Didymos. Yellow indicates regions where stress is greater than yield stress. The spin axis is along the vertical direction. **a** and **b** show the solution at a spin period of 2.26 h whereas **c** and **d** show the solution for a 3.5 h period. **a and c** show stress on a cross section through the center, while **b** and **d** show stress on the surface of the asteroid. The arrows indicate the total deformation vectors and their lengths are proportional to magnitudes of stress. (For interpretation of the references to colour in this figure legend, the reader is referred to the web version of this article.)

900 KW and 450 KW, respectively.

The peak Goldstone SNRs in 2022 will be about 10 per run around the time of the close approach to Earth. This is strong enough to detect the primary with Doppler-only echo power spectra and coarse-resolution delay-Doppler images. Monostatic observations could provide a resolution of 150 m/pixel, which is twice as coarse as the finest Goldstone images obtained in 2003. Echoes from the secondary will be weak but should be detectable using integrations over at least several transmit/receive cycles. Goldstone observations in 2022 will not resolve the secondary because the SNRs will be too weak. View periods at Goldstone during the dates with the strongest SNRs vary from 3 to 7.5 h. Thus, observations in early October could cover one full rotation by the primary and about one fourth of a revolution by the secondary. By mid-October, Goldstone observations could cover somewhat more than half of a revolution by the secondary and three rotations by the primary. This assumes that observations occur during the entire interval when the asteroid is at least 20° above the horizon at Goldstone. After mid-October, the SNRs for the secondary at Goldstone will drop below the threshold for detection. Time at Goldstone has already been requested but the detailed schedule will not be available until the summer of 2022.

We can increase the Goldstone SNRs by at least a factor of two by receiving at the Green Bank Telescope. This should improve the range resolution by a factor of two to 75 m/pixel on dates when the asteroid is closest and match the finest range resolution obtained at Goldstone in 2003. Due to the southern declinations of Didymos and the longitude and latitude differences between Goldstone and GBT, the first date when reception of Goldstone transmissions is possible at GBT is on October 1, the day after the nominal DART impact date.

Didymos enters the declination window at Arecibo on October 24, about three weeks after the DART impact (Tables A2 and A4). The primary will be detectable with SNRs of about 70 per run from late October to early January and the satellite will be detectable at SNRs greater than about two per round-trip light time from late October until early December. If the DART impact occurs on September 30, then it should be possible to use radar observations to check for orbital changes for about 2 months after impact before the SNRs become too weak.

The lengths of the observing tracks at Arecibo will vary from a minimum of 40 min on October 24 to a maximum of 2.8 h in late November. After late November the view periods will gradually shrink to about 2.3 h by early January. The SNR/run will be about seven times stronger than the SNRs at Goldstone but only 1/3 as strong as they were at Arecibo in 2003. Consequently, Arecibo images in 2022 will be less detailed than in 2003, when the finest resolution was 15 m/pixel, but should still achieve a resolution of 30 m/pixel that will place >100 pixels on the primary and show moderate levels of detail. Echoes from the secondary could show 2–3 pixels in time delay and will be too weak for detailed imaging. These images will not show changes to the surface of the satellite due to the impact, which are expected to be on scales that are much smaller than the radar imaging resolution.

If the orbital period of the secondary changes by 1% due to the DART impact, then the rate of change of the orbital phase of the secondary with respect to the no-impact case would be about 7°/day, which corresponds to ~140 m/day change in the secondary's position along its orbit. Depending on the orbital phase at the time of observation and the observing geometry, this change could be detectable within a few days of observations at Goldstone and easily at Arecibo. Good knowledge of the pre-impact orbit, which can be obtained by radar observations for a few days at Goldstone and optical observations for several weeks before the impact, will be necessary to measure the drift in orbital phase due to impact.

After 2022, the next opportunity for radar observations of Didymos with existing facilities will be in October 2062, during an approach within 0.050 au, when the SNRs at Goldstone and Arecibo or equivalent facilities should be comparable to those obtained in 2003.

Acknowledgements

Appendix A. Supplementary data

Supplementary data to this article can be found online at https://doi.org/10.1016/j.icarus.2020.113777.

References

Becker, T.M., Howell, E.S., Nolan, M.C., Magri, C., Pravec, P., Taylor, P.A., Oey, J., Higgins, D., Viági, J., Kornoš, L., Galád, A., Gajdoš, Š., Gaftonyuk, N.M., Krugly, Y. N., Molotov, I.E., Hicks, M.D., Carbognani, A., Warner, B.D., Vachier, F., Marchis, F., Pollock, J.T., 2015. Physical modeling of triple near-Earth Asteroid (153591) 2001 SN263 from radar and optical light curve observations. Icarus 248, 499–515.

Benner, L.A.M., Ostro, S.J., Magri, C., Nolan, M.C., Howell, E.S., Giorgini, J.D., Jurgens, R.F., Margot, J.L., Taylor, P.A., Busch, M.W., Shepard, M.K., 2008. Near-Earth asteroid surface roughness depends on compositional class. Icarus 198, 294–304.

Benner, L.A.M., Busch, M.W., Giorgini, J.D., Taylor, P.A., Margot, J.L., 2015. Radar observations of near-Earth and main-belt asteroids. In: Michel, P., DeMeo, F.E., Bottke, W.F. (Eds.), Asteroids IV. Univ. of Arizona Press, Tucson, pp. 165–182.

Brozović, M., Benner, L.A.M., Taylor, P.A., Nolan, M.C., Howell, E.S., Magri, C., Scheeres, D.J., Giorgini, J.D., Pollock, J.T., Pravec, P., Galád, A., Fang, J., Margot, J. L., Busch, M.W., Shepard, M.K., Reichart, D.E., Ivarsen, K.M., Haislip, J.B., LaCluyze, A.P., Jao, J., Slade, M.A., Lawrence, K.J., Hicks, M.D., 2011. Radar and optical observations and physical modeling of triple near-Earth asteroid (136617) 1994 CC. Icarus 216, 241–256.

Busch, M.W., Benner, L.A.M., Ostro, S.J., Giorgini, J., Jurgens, R.F., Rose, R., Scheeres, D. J., Magri, C., Margot, J.L., Nolan, M.C., Hine, A.A., 2008. Physical properties of near-Earth Asteroid (33342) 1998 WT24Show affiliations. Icarus 195 (2), 614–621. https://doi.org/10.1016/j.icarus.2008.01.020.

Busch, M.W., Ostro, S.J., Benner, L.A.M., Brozovic, M., Giorgini, J.D., Jao, J.S., Scheeres, D.J., Magri, C., Nolan, M.C., Howell, E.S., Taylor, P.A., Margot, J.L., Brisken, W., 2011. Radar observations and the shape of near-Earth asteroid 2008 EV5. Icarus 212, 649–660.

Chen, W.F., Han, D., 2007. Plasticity for Structural Engineers. J. Ross Publishing, Plantation, Florida.

Cheng, A.F., Michel, P., Jutzi, M., Rivkin, A.S., Stickle, A., Barouin, O., Ernst, C., Atchison, J., Pravec, P., Richardson, D.C., 2016. Asteroid impact and deflection assessment mission: kinetic impactor. Planet. Space Sci. 121, 27–35.

Cheng, A.F., Rivkin, A.S., Michel, P., Atchison, J., Barnouin, O., Benner, L., Chabot, N.L., Ernst, C., Fahnestock, E.G., Kueppers, M., Pravec, P., Rainey, E., Richardson, D.C., Stickle, A.M., Thomas, C., 2018. AIDA DART asteroid deflection test: planetary defense and science objectives. Planet. Space Sci. 157, 104–115.

Chesley, S.R., Ostro, S.J., Vokrouhlický, D., Čapek, D., Giorgini, J.D., Nolan, M.C., Margot, J.L., Hine, A.A., Benner, L.A.M., Chamberlin, A.B., 2003. Direct detection of the Yarkovsky effect by radar ranging to asteroid 6489 Golevka. Science 302, 1739–1742.

De Leon, J., Licandro, J., Serra-Ricart, M., Pinilla-Alonso, N., Campins, H., 2010. Observations compositional, and physical characterization of near-Earth and Marscrosser asteroids from a spectroscopic survey. A&A 517, A23. https://doi.org/10.1051/0004-6361/200913852.

Fang, J., Margot, J.L., 2012. Near-Earth binaries and triples: origin and evolution of spin-orbital properties. Astron. J. 143, 24.

Fowler, J.W., Chillemi, J.R., 1992. Philips laboratory technical report PL-TR-92-2049. Jet Propulsion Laboratory, Pasadena, California 17.

Fujiwara, A., Kawaguchi, J., Yeomans, D.K., Abe, M., Mukai, T., Okada, T., Saito, J., Yano, H., Yoshikawa, M., Scheeres, D.J., Barnouin-Jha, O., Cheng, A.F., Demura, H., Gaskell, R.W., Hirata, N., Ikeda, H., Kominato, T., Miyamoto, H., Nakamura, A.M., Nakamura, R., Sasaki, S., Uesugi, K., 2006. The rubble-pile asteroid Itokawa as observed by Hayabusa. Science 312, 1330–1334.

Harmon, J.K., Nolan, M.C., Ostro, S.J., Campbell, D.B., 2004. Radar studies of comet nuclei and grain comae. In: Festou, M.C., Keller, H.U., Weaver, H.A. (Eds.), Comets II. Univ. of Arizona Press, Tucson, pp. 265–279.

Harris, A.W., Fahnestock, E.G., Pravec, P., 2009. On the shapes and spins of "rubble pile" asteroids. Icarus 199, 310–318.

Hirabayashi, M., 2015. Failure modes and conditions of a cohesive, spherical body due to YORP spin-up. Mon. Not. R. Astron. Soc. 454, 2249–2257.

Hirabayashi, M., Scheeres, D.J., 2014. Stress and failure analysis of rapidly rotating asteroid (29075) 1950 DA. Astrophys. J. Lett. 798, L8.

Hirabayashi, M., Scheeres, D.J., 2019. Rotationally induced failure of irregularly shaped asteroids. Icarus 317, 354–364.

Hirabayashi, M., Scheeres, D.J., Chesley, S.R., Marchi, S., McMahon, J.W., Steckloff, J., Mottola, S., Naidu, S.P., Bowling, T., 2016. Fission and reconfiguration of bilobate comets as revealed by 67P/Churyumov–Gerasimenko. Nature 534, 352–355.

Hirabayashi, M., Schwartz, S.R., Yu, Y., Davis, A.B., Chesley, S.R., Fahnestock, E.G., Michel, P., Richardson, D.C., Naidu, S.P., Scheeres, D.J., Cheng, A.F., 2017. Constraints on the perturbed mutual motion in Didymos due to impact-induced deformation of its primary after the DART impact. Mon. Not. Roy. Astron. Soc. 472, 1641–1648.

Hirabayashi, M., Tatsumi, E., Miyamoto, H., Komatsu, G., Sugita, S., Watanabe, S., Scheeres, D.J., Barnouin, O.S., Michel, P., Honda, C., Michikami, T., Cho, Y., Morota, T., Hirata, N., Hirata, N., Sakatani, N., Schwartz, S.R., Honda, R., Yokota, Y., Kameda, S., Suzuki, H., Kouyama, T., Hayakawa, M., Matsuoka, M., Ogawa, K., Sawada, H., Yoshikawa, M., Tsuda, Y., 2019. The Western bulge of 162173 Ryugu formed as a result of a rotationally driven deformation process. Astrophys. J. Lett. 874, L10.

Huang, J., Ji, J., Ye, P., Wang, X., Yan, J., Meng, L., Wang, S., Li, C., Li, Y., Qiao, D., Zhao, W., 2013. The ginger-shaped asteroid 4179 Toutatis: new observations from a successful flyby of Chang'e-2. Sci. Rep. 3, 3411.

Hudson, S., 1993. Three-dimensional reconstruction of asteroids from radar observations. Remote Sens. Rev. 8, 195–203.

Lambe, T.W., Whitman, R., 2008. Soil Mechanics. John Wiley & Sons.

Lauretta, D.S., DellaGiustina, D.N., Bennett, C.A., Golish, D.R., Becker, K.J., Balram-Knutson, S.S., Barnouin, O.S., Becker, T.L., Bottke, W.F., Boynton, W.V., Campins, H., 2019. The unexpected surface of asteroid (101955) Bennu. Nature 568, 55–60. https://doi.org/10.1038/s41586-019-1033-6.

Magri, C., Ostro, S.J., Scheeres, D.J., Nolan, M.C., Giorgini, J.D., Benner, L.A.M., Margot, J.L., 2007. Radar observations and a physical model of asteroid 1580 Betulia. Icarus 186, 152–177.

Margot, J.L., Nolan, M.C., Benner, L.A.M., Ostro, S.J., Jurgens, R.F., Giorgini, J.D., Slade, M.A., Campbell, D.B., 2002. Binary asteroids in the near-earth object population. Sci 296, 1445.

Margot, J.L., Pravec, P., Taylor, P., Carry, B., Jacobson, S., 2015. Asteroid aystems: binaries, triples, and pairs. In: Michel, P., DeMeo, F.E., Bottke, W.F. (Eds.), Asteroids IV, pp. 355–374.

Michel, P., Cheng, A., Kuppers, M., Pravec, P., Blum, J., Delbo, M., Green, S.F., Rosenblatt, P., Tsiganis, K., Vincent, J.B., Biele, J., Ciarletti, V., Herique, A., Ulamec, S., Carnelli, I., Galvez, A., Benner, L.A.M., Naidu, S.P., Barnouin, O.S., Richardson, D.C., Rivkin, A., Scheirich, P., Moskovitz, N., Thirouin, A., Schwartz, S. R., Campo Bagatin, A., Yu, Y., 2016. Science case for the Asteroid Impact Mission (AIM): a component of the Asteroid Impact & Deflection Assessment (AIDA) mission. Adv. Space Res. 57, 2529–2547.

Michel, P., Kueppers, M., Sierks, H., Carnelli, I., Cheng, A.F., Mellab, K., Granvik, M., Kestilä, A., Kohout, T., Muinonen, K., Näsilä, A., 2018. European component of the AIDA mission to a binary asteroid: characterization and interpretation of the impact of the DART mission. Adv. Space Res. 62, 2261–2272.

Minton, D.A., 2008. The topographic limits of gravitationally bound, rotating sand piles. Icarus 195, 698–704.

Naidu, S.P., Margot, J.L., Taylor, P.A., Nolan, M.C., Busch, M.W., Benner, L.A.M., Brozovic, M., Giorgini, J.D., Jao, J.S., Magri, C., 2015. Radar imaging and characterization of the binary near-Earth asteroid (185851) 2000 DP107. Astron. J. 150, 54.

Nolan, M.C., Magri, C., Howell, E.S., Benner, L.A.M., Giorgini, J.D., Hergenrother, C.W., Hudson, R.S., Lauretta, D.S., Margot, J.L., Ostro, S.J., Scheeres, D.J., 2013. Shape model and surface properties of the OSIRIS-REx target asteroid (101955) Bennu from radar and lightcurve observations. Icarus 226, 629–640.

Ostro, S.J., 1993. Planetary radar astronomy. Rev. Mod. Phys. 65, 1235–1279.

Ostro, S.J., Margot, J.L., Benner, L.A.M., Giorgini, J.D., Scheeres, D.J., Fahnestock, E.G., Broschart, S.B., Bellerose, J., Nolan, M.C., Magri, C., Pravec, P., Scheirich, P., Rose, R., Jurgens, R.F., De Jong, E.M., Suzuki, S., 2006. Radar imaging of binary near-Earth asteroid (66391) 1999 KW4. Science 314, 1276–1280.

Peale, S., 1969. Generalized Cassini's laws. Astron. J. 74, 483–489.

Pirrotta, S., Simonetti, S., Di Tana, V., Cotugno, B., Amoroso, M., Dotto, E., Mazzotta Epifani, E., Della Corte, V., Lavagna, M., Capannolo, A., Pesce, V., Gai, I., Tortora, P., Zannoni, M., 2019. LICIACube, the light Italian CubeSat for imaging of asteroid joining NASA DART mission to Didymos binary system. In: EGU General Assembly Conference Abstract id. 17780.

Pravec, P., Harris, A.W., 2007. Binary asteroid population. 1. Angular momentum content. Icarus 190, 250–259.

Pravec, P., Scheirich, P., 2018. Binary asteroid (65803) Didymos: Observations of and constraints on the binary system. In: 42nd COSPAR Scientific Assembly (id S.3-4-18).

Pravec, P., Harris, A.W., Michalowski, T., 2002. Asteroid rotations. In: Bottke Jr., W.F., Cellino, A., Paolicchi, P., Binzel, R.P. (Eds.), Asteroids III. Univ. of Arizona Press, Tucson, pp. 113–122.

Pravec, P., Benner, L.A.M., Nolan, M.C., Kusnirak, P., Pray, D., Giorgini, J.D., Jurgens, R. F., Ostro, S.J., Margot, J.L., Magri, C., Grauer, A., Larson, S., 2003. (65803) 1996 GT. IAU Circ. No. 8244.

Pravec, P., Scheirich, P., Kusnirak, P., Sarounova, L., Mottola, S., Hahn, G., Brown, P., Esquerdo, G., Kaiser, N., Krzeminski, Z., Pray, D.P., Warner, B.D., Harris, A.W., Nolan, M.C., Howell, E.S., Benner, L.A.M., Margot, J.L., Galad, A., Holliday, W., Hicks, M.D., Krugly, Y.N., Tholen, D., Whiteley, R., Marchis, F., DeGraff, D.R., Grauer, A., Larson, S., Velichko, F.P., Cooney, W.R., Stephens, R., Zhu, J., Kirsch, K., Dyvig, R., Snyder, L., Reddy, V., Moore, S., Gajdos, S., Vilagi, J., Masi, G., Higgins, D., Funkhouser, G., Knight, B., Slivan, S., Behrend, R., Grenon, M., Burki, G., Roy, R., Demeautis, C., Matter, D., Waelchli, N., Revaz, Y., Klotz, A., Rieugne, M., Thierry, P., Cotrez, V., Brunetto, L., Kober, G., 2006. Photometric survey of binary near-Earth asteroids. Icarus 181, 63–93.

Pravec, P., Harris, A.W., Kušnirák, P., Galád, A., Hornoch, K., 2012. Absolute magnitudes of asteroids and a revision of asteroid albedo estimates from WISE thermal observations. Icarus 221, 365–387.

Pravec, P., Scheirich, P., Kušnirák, P., Hornoch, K., Galád, A., Naidu, S.P., Pray, D.P., Világi, J., Gajdoš, Š., Kornoš, L., Krugly, Y.N., et al., 2016. Binary asteroid population. 3. Secondary rotations and elongations. Icarus 267, 267–295.

Saito, J., Miyamoto, H., Nakamura, R., Ishiguro, M., Michikami, T., Nakamura, A.M., Demura, H., Sasaki, S., Hirata, N., Honda, C., Yamamoto, A., 2006. Detailed images of asteroid 25143 Itokawa from Hayabusa. Science 312, 1341–1344.

Scheirich, P., Pravec, P., 2009. Modeling of lightcurves of binary asteroids. Icarus 200, 531–547.

Shepard, M.K., Margot, J.L., Magri, C., Nolan, M.C., Schlieder, J., Estes, B., Bus, S.J., Volquardsen, E.L., Rivkin, A.S., Benner, L.A.M., Giorgini, J.D., 2006. Radar and infrared observations of binary near-Earth asteroid 2002 CE26. Icarus 184, 198–210.

Taylor, P.A., 2009. Tidal Interactions in Binary Asteroid Systems. PhD Thesis. Cornell University (ISBN: 9781109230994).

Tortora, P., Di Tana, V., 2019. LICIACube, the Italian witness of DART impact on Didymos. In: IEEE 5th International Workshop on Metrology for AeroSpace (MetroAeroSpace), pp. 314–317.

Veverka, J., Thomas, P.C., Bell, J.F., Bell, M., Carcich, B., Clark, B., Harch, A., Joseph, J., Martin, P., Robinson, M., Murchie, S., 1999. Imaging of asteroid 433 Eros during NEAR's flyby reconnaissance. Science 285, 562–564.

Virkki, A., Muinonen, K., 2016. Radar scattering by planetary surfaces modeled with laboratory-characterized particles. Icarus 269, 38–49.

Walsh, K.J., Richardson, D.C., Michel, P., 2008. Rotational breakup as the origin of small binary asteroids. Nature 454, 188–191.

Walsh, K.J., Richardson, D.C., Michel, P., 2012. Spin-up of rubble-pile asteroids: disruption, satellite formation, and equilibrium shapes. Icarus 220, 514–529.

Watanabe, S., Hirabayashi, M., Hirata, N., Noguchi, R., Shimaki, Y., Ikeda, H., Tatsumi, E., Yoshikawa, M., Kikuchi, S., Yabuta, H., Nakamura, T., 2019. Hayabusa2 arrives at the carbonaceous asteroid 162173 Ryugu—a spinning top–shaped rubble pile. Science 364, 268–272.

Werner, R.A., Scheeres, D.J., 1997. Exterior gravitation of a polyhedron derived and compared with harmonic and mascon gravitation representations of asteroid 4769 Castalia. Celestial Mech. Dyn. Astron. 65, 313–344.

Yeomans, D.K., Antreasian, P.G., Barriot, J.-P., Chesley, S.R., Dunham, D.W., Farquhar, R.W., Giorgini, J.D., Helfrich, C.E., Konopliv, A.S., McAdams, J.V., Miller, J.K., Owen, W.M., Scheeres, D.J., Thomas, P.C., Veverka, J., Williams, B.G., 2000. Radio science results during the NEAR-shoemaker spacecraft rendezvous with Eros. Science 289, 2085–2088.

Zhang, Y., Richardson, D.C., Barnouin, O.S., Maurel, C., Michel, P., Schwartz, S.R., Ballouz, R.L., Benner, L.A.M., Naidu, S.P., Li, J., 2017. Creep stability of the proposed AIDA mission target 65803 Didymos: I. Discrete cohesionless granular physics model. Icarus 294, 98–123.

Zhang, Y., Richardson, D.C., Barnouin, O.S., Michel, P., Schwartz, S.R., Ballouz, R.L., 2018. Rotational failure of rubble-pile bodies: influences of shear and cohesive strengths. Astrophys. J. 857, 15.